J. Fluid Mech. (2002), *vol.* 471, *pp.* 285–314. © 2002 Cambridge University Press
DOI: 10.1017/S0022112002002124 Printed in the United Kingdom

Sound generation by a two-dimensional circular cylinder in a uniform flow

By OSAMU INOUE AND NOZOMU HATAKEYAMA

Institute of Fluid Science, Tohoku University, 2-1-1 Katahira, Aoba-ku, Sendai 980-8577, Japan

(Received 9 October 2000 and in revised form 25 June 2002)

The sound generated by a circular cylinder in a flow at low Mach numbers is investigated by direct solution of the two-dimensional unsteady compressible Navier–Stokes equations. Results show that sound pressure waves are generated primarily by vortex shedding from the cylinder surface into its wake. When a vortex is shed from one side of the cylinder, a negative pressure pulse is generated from that side whereas a positive pressure pulse is generated from the other side; alternate vortex shedding from the upper and lower sides of the cylinder produces negative and positive pulses alternately and thus produces sound pressure waves on both sides. The dipolar nature of the generated sound is confirmed; lift dipole dominates the sound field. The Doppler effect is shown to play an important role at finite Mach numbers. The direct solutions are also compared with the solutions obtained by Curle's acoustic analogy. The results show that Curle's solution describes well not only the generation mechanism of the sound but also the propagation process if we take the Doppler effect into consideration.

1. Introduction

Since the work of Strouhal (1878) on aeolian tones, the flow around a circular cylinder has been one of the major topics in fluid mechanics. The flow contains fundamentally important fluid mechanics problems, such as forces acting on a body (lift, drag), transition to turbulence, aerodynamic noise, etc. A number of studies of the flow around a circular cylinder have been made experimentally, theoretically and computationally. For recent review articles, readers are referred to Oertel (1990) and Williamson (1996), among others.

The sound generated by the flow around a circular cylinder has also been studied by many investigators. Strouhal (1878) experimentally found that the frequency f of the sound radiated from a cylinder of diameter D is related to the velocity U_∞ of a uniform flow as $fD/U_\infty = \text{const}$. The constant is now known as the Strouhal number, St, and is 0.20–0.22 for the Reynolds number range $300 \leqslant Re \leqslant 10^4$. Rayleigh (1896) recognized that the production of the sound is connected with the instability of the vortex sheets in the cylinder wake (Kármán vortex street). It is now known that the frequency f of the sound is the same as the shedding frequency of vortices from the cylinder into its wake (Gerrard 1955).

Since the pioneering paper of Lighthill (1952), most theoretical works on sound have used an acoustic analogy. For comprehensive reviews, readers are referred to Ffowcs Williams (1969, 1977, 1996). The sound radiated from a cylinder has also been studied using an acoustic analogy (Curle 1955; Phillips 1956; Etkin, Korbacher & Keefe 1957). Curle (1955) extended Lighthill's acoustic analogy to include the

https://doi.org/10.1017/S0022112002002124 Published online by Cambridge University Press

influence of solid boundaries on the sound field, showing that boundary terms could provide effective mass and momentum injection into the flow, acoustically equivalent to monopole and dipole sources of fundamentally greater acoustic efficiency than Lighthill's volume quadrupoles. Curle predicted that at the low speeds at which a Kármán vortex street is obtained the sound is not generated principally by the quadrupoles but that dipole sound dominates the sound field. Curle also predicted that the sound associated with the drag force has double the frequency of vortex shedding while that associated with the lift force has the same frequency.

Based on the Curle's acoustic analogy, Phillips (1956) calculated the fluctuations in lift and drag upon a circular cylinder at Reynolds numbers between 40 and 160, and found that the fluctuations in lift per unit length are much greater than the fluctuations in drag, indicating the directional distribution of sound intensity. Etkin *et al.* (1957) obtained a similar result to those of Curle and Phillips.

Gerrard (1955) experimentally found that the sound field is a dipole field with the direction of the dipole at right angles to the flow direction, in agreement with Curle (1955), Phillips (1956) and Etkin *et al.* (1957).

Work in the field of computational aeroacoustics (CAA) can be categorized into three groups. The first group makes use of an acoustic analogy. The acoustic analogies proposed by Lighthill and Curle relate sound exactly to integrals of surface and volume source terms. Therefore, once the source terms are known, the sound field is calculated by using the acoustic analogy. In the analyses of the first group, numerical simulations are separated into two parts: the near-field aerodynamic part and the far-field acoustic part. First, in the aerodynamic part, near-field flow structures are simulated by using computational fluid dynamics (CFD) techniques. Incompressible Navier–Stokes simulations are often used for low-Mach-number flows. Then, in the acoustic part, the far-field sound is calculated from an acoustic analogy. The source terms are evaluated using the near-field flow quantities. This method, often called the hybrid method, saves computational time as well as memory storage compared with direct numerical simulations (DNS), because the flow in the far field is assumed to be stationary or uniform and thus not solved numerically (Hardin & Lamkin 1984; Mankbadi, Hayder & Povinelli 1994; Wang, Lele & Moin 1996(*a*, *b*); Cox, Brentner & Rumsey 1998).

Wang *et al.* (1996*a*) studied sound generated by vortex shedding in a two-dimensional, low-Mach-number laminar flow past a NACA 0012 airfoil at a chord Reynolds number of 10^4. The incompressible Navier–Stokes equations were solved to give an approximate description of the near-field flow dynamics and the acoustic source terms. The far-field sound was computed based on Curle's acoustic analogy. The results showed that the quadrupole sound is weak compared with the sound due to lift and drag dipoles when the Mach number is small.

In order to study sound generated by uniform flow past a cylinder for a range of Reynolds number from 100 to 5×10^6, Cox *et al.* (1998) solved, for the near field, the two-/three-dimensional compressible, Reynolds-averaged Navier–Stokes equations by a finite volume method, which is second-order accurate both in space and time. The Mach number prescribed was 0.2. The far-field sound was obtained by Lighthill's analogy, using the Ffowcs Williams–Hawkings equations. The results showed that the quadrupolar component of sound is significantly smaller than the dipole. They also point out that sound computation is highly dependent on the accuracy of the near-field flow quantities produced by the CFD calculation. Some of the recent work, falling into the first group, on the sound generation due to flow past a circular cylinder can be found in Tam & Hardin (1997).

https://doi.org/10.1017/S0022112002002124 Published online by Cambridge University Press

The second group makes use of a different method, called the acoustic/viscous splitting method (Hardin & Pope 1994), to study the sound generation by a cylinder in a uniform flow (Pope 1997; Shen & Sørensen 1999; Slimon, Soteriou & Davis 1999). This method splits the computation into two parts, as in the above-mentioned hybrid method, but does not use acoustic analogies. Instead, flow quantities are represented, under the assumption of low Mach number, by an incompressible mean flow and a perturbation about the mean. First, incompressible viscous equations for mean flow quantities are solved. Then, using the mean quantities, perturbation equations are solved. In the near field, the perturbation quantities represent the difference between the fully compressible flow and the assumed incompressible mean flow. In the far field, the perturbation quantities are equivalent to acoustic quantities. Shen & Sørensen (1999) applied this method to the flow past a circular cylinder at a Reynolds number of 200 and a Mach number of 0.2. The result showed that the pressure waves propagate from the cylinder along the normal direction of the flow. The acoustic/viscous splitting method may possibly be an effective and convenient method of predicting acoustic fields resulting from low-Mach-number, non-compact source regions (Slimon *et al.* 1999). So far the results obtained by this method are qualitative, and detailed descriptions of the acoustic field produced by the cylinder have not yet been given. Hansen, Long & Morris (2000) proposed a novel method in which the mean flow may not be restricted to low Mach numbers.

The third group makes use of direct numerical simulations (DNS), where both the fluid motion and the sound which it generates are directly computed (Colonius, Lele & Moin 1994, 1997; Mitchell, Lele & Moin 1995, 1999; Inoue & Hattori 1999; Inoue 2000; Inoue, Hattori & Sasaki 2000; Inoue & Takahashi 2000). For comprehensive reviews, readers are referred to Tam (1995), Lele (1997) and Moin & Mahesh (1998). In these simulations, the Navier–Stokes equations are solved by using highly accurate schemes both for space and time in order to precisely capture the sound pressure, which is usually much smaller than the pressure in the near field. One of the advantages of DNS over the methods in the first two groups is its capability in clarifying the generation and propagation processes of the sound in the near and intermediate fields, without suffering from restrictions such as low Mach number, high Reynolds number and compactness of the source region. So far most of the computational work on the sound generation due to flow past a circular cylinder has been done using the hybrid or acoustic/viscous splitting methods, and the studies using DNS are very few. This is mainly because DNS requires a large amount of computer resources.

Our purpose in this paper is to study, using DNS over the entire region from the near to far fields, the generation and propagation mechanisms of the sound produced by a two-dimensional circular cylinder in a uniform flow, and to increase our understanding of the characteristic features of the sound. One of the goals of this study is to clarify the relation between the vortex/flow dynamics and the sound pressure waves it generates. The effect of the Mach number is also examined. The present DNS results are also compared with the prediction based on Curle's acoustic analogy, which is widely used in the hybrid method (for example, Wang *et al.* 1996*a*; You *et al.* 1998; Manoha, Troff & Sagaut 2000).

2. Mathematical formulation and numerical procedure

2.1. *Flow model and parameters*

A schematic diagram of the flow model is presented in figure 1. A cylinder is fixed at the origin, and the coordinates parallel and normal to the free stream are denoted

https://doi.org/10.1017/S0022112002002124 Published online by Cambridge University Press

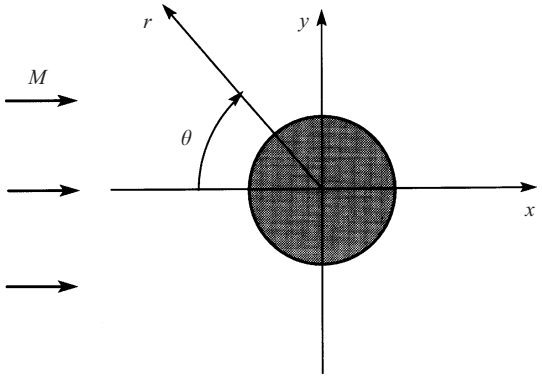


FIGURE 1. Schematic diagram of the flow model.

as x and y, respectively. The Mach number, M, of the uniform flow is defined by $M = U_\infty/c_\infty$. Here, U_∞ denotes the velocity of the uniform flow and c_∞ denotes the speed of sound. The lengths are made dimensionless by the diameter D of the cylinder. The velocity is scaled by c_∞. The Reynolds number is defined as $Re = U_\infty D/v_\infty$, where v_∞ is the kinematic viscosity. In this study, the Mach number is prescribed to be $M = 0.05$ to 0.3. Since the Mach number is relatively low, temperature dependence of the transport properties is not likely to be a significant effect (Colonius *et al.* 1997). Therefore, the molecular viscosity and the thermal conductivity are taken to be constant. The Prandtl number is assumed to be 0.75, and the ratio of specific heats is 1.4. According to experiments (Cimbala, Nagib & Roshko 1988), cylinder wakes with Re larger than 160 become irregular and eventually turbulent; two-dimensional computation may be most meaningful for a flow with $Re \leqslant 160$. At the same time, Re must be large enough for vortex shedding to occur, because it is essential for the sound generation. In this paper, the Reynolds number is fixed to be $Re = 150$.

2.2. *Numerical schemes and computational parameters*

The two-dimensional unsteady compressible Navier–Stokes equations are solved by a finite difference method. For spatial derivatives, a sixth-order-accurate compact Padé scheme (fourth-order-accurate at the boundaries) proposed by Lele (1992) is adopted. The fourth-order Runge–Kutta scheme is used for time-integration.

In this study, we adopt an O-grid system with non-uniform meshes. The computational domain is divided into three regions of different grid spacings: a surface region $[0.5 \leqslant r \leqslant r_{surface}, -\pi \leqslant \theta \leqslant \pi]$, a sound region $[r_{surface} \leqslant r \leqslant r_{sound}, -\pi \leqslant \theta \leqslant \pi]$, and a buffer region $[r_{sound} \leqslant r \leqslant r_{buffer}, -\pi \leqslant \theta \leqslant \pi]$. The spacing in the surface region is prescribed to be fine enough to analyse the boundary layer on the cylinder surface. In the sound region, the spacing is prescribed to be larger than that in the surface region, but still small enough to capture sound pressure waves. The spacing in the buffer region is prescribed such that pressure waves damp with increase in distance and become sufficiently small before reaching the outer boundary of the computational domain where the non-reflecting boundary conditions are used. The role of the buffer region is similar to that of the 'sponge region' of Colonius *et al.* (1997). Only the results obtained in the surface and sound regions are used for analysis. The spacings among the three regions are connected smoothly by using hyperbolic-tangent curves. In addition, we imposed a restriction that the increment of the spacing does not exceed 4% in the surface and sound regions, and 9% in the buffer region. A typi-

https://doi.org/10.1017/S0022112002002124 Published online by Cambridge University Press

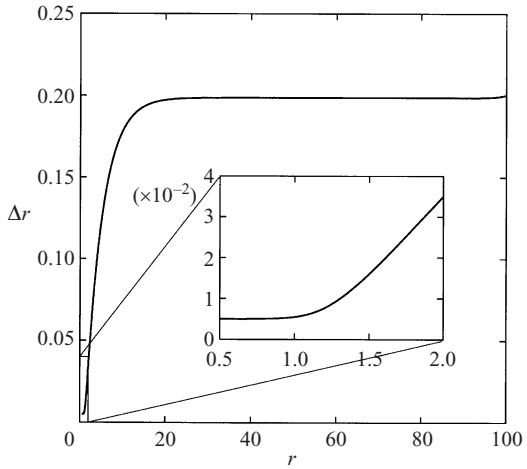


FIGURE 2. Example of the distribution of grid spacing against r. $r_{surface} = 1$, $r_{sound} = 100$, $r_{buffer} = 1500$.

cal example of the distribution of grid spacing in the surface and sound regions is presented against r in figure 2, where $r_{surface} = 1.0$, $r_{sound} = 100$ and $r_{buffer} = 1500$. The spacings are $\Delta r_{min} = 0.005$ adjacent to the cylinder surface, $\Delta r_{sound} = 0.2$ at $r = r_{sound}$, and $\Delta r_{buffer} = 20.0$ at $r = r_{buffer}$. The spacing in the θ-direction was prescribed to be uniform.

Adiabatic and no-slip conditions were adopted on the cylinder surface, and non-reflecting boundary conditions (Poinsot & Lele 1992) were used at the outer boundary of the buffer region, $r = r_{buffer}$.

After many preliminary tests, the grid spacings and the sizes of the three regions were determined as follows.

$$\Delta r_{min} = 0.005,\ \Delta r_{sound} = 0.2,\ \Delta r_{buffer} = 20.0,\ \Delta\theta = 0.72^{\circ}.$$

$$r_{surface} = 1.0,\ r_{sound} = 100,\ r_{buffer} = 1500.$$

Grid- and domain-size independence has been established for the solutions presented in this paper. The total number of grid points is 871 (r-direction) $\times$ 503 (θ-direction), in which 160×503 grid points are distributed in the buffer region. With this grid distribution, the number of grid points within the boundary layer for $Re = 150$ is 16 in the r-direction. (The thickness of the boundary layer was estimated by $\delta \sim 1/\sqrt{Re}$, and $\delta \sim 0.08$ for $Re = 150$.) The time step is $\Delta t = 0.002$.

2.3. *Initial conditions*

Initial flow fields were given by potential flows except for the boundary layer on the cylinder surface. For the boundary layer, a tangent-hyperbolic filter was applied such that both the non-slip condition on the surface and the potential flow condition at the boundary layer edge are satisfied. At the initial stage of time evolution, the wake develops symmetrically with respect to the x-axis. In order to achieve an earlier transition to the asymmetric Kármán vortex street, a Taylor-type vortex was superimposed on the flow (at $x = 2.0$, $y = 0$) at an initial instant ($t = 25$) as a perturbation. With increased time, the vortex is convected away to the buffer region with decreasing strength due to the viscous effect, and then dies out; data acquisition was set forth sufficiently after the effect of the initial perturbation became negligible (typically $t \geqslant 1000$).

https://doi.org/10.1017/S0022112002002124 Published online by Cambridge University Press

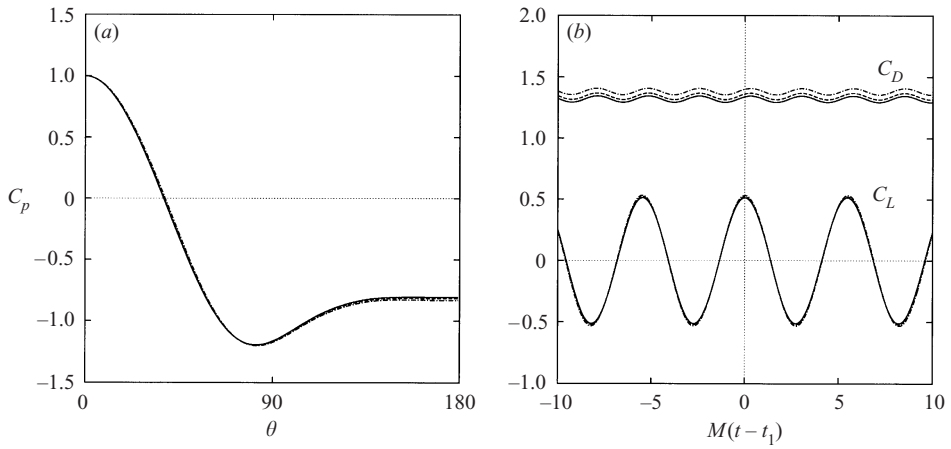


FIGURE 3. Effect of the Mach number on force coefficients. $Re = 150$. (a) Time-averaged pressure coefficient C_p, (b) lift coefficient C_L and drag coefficient C_D: ——, $M = 0.1$; – – – –, $M = 0.2$; – · – · –, $M = 0.3$.

3. Results and discussion

3.1. *Near-field structure and generation of pressure waves*

Forces acting on the cylinder are presented in figure 3 for three different Mach numbers ($M = 0.1$, 0.2 and 0.3), in terms of the mean pressure coefficient C_p, lift coefficient C_L and drag coefficient C_D. In figure 3(b), time variations of C_L and C_D are plotted against the reduced time $M(t - t_1)$, where $t_1(M)$ is the time of a peak value, because the near-field flow structures may be more adequately described by the time scale D/U_∞ than D/c_∞. Figure 3 shows that the coefficients C_p and C_L are not affected significantly by the Mach number, but C_D increases with increasing M. The mean value of C_D at $M = 0.1$ is 1.32, which is equal to the value obtained computationally by Kwon & Choi (1996) for incompressible flows at $Re = 140$ and 160 (see also Park, Kwon & Choi 1998). The amplitude of C_L is approximately 0.52, irrespective of M, which is close to the values of Kwon & Choi (1996) where the amplitude of C_L is 0.48 at $Re = 140$ and 0.55 at $Re = 160$. The Strouhal number St in figure 3 is 0.183, irrespective of M, which is close to the experimental values (0.18 at $Re = 150$ in Williamson 1989; 0.185 at $Re = 155$ in Williamson & Prasad 1993), and fits very well the empirical line, $St = 0.2684 - 1.0356(Re)^{-1/2}$, proposed by Fey, König & Eckelmann (1998) for the vortex shedding from a circular cylinder. The Strouhal number in this study is also close to the computational values for incompressible flows (0.181 at $Re = 140$ and 0.187 at $Re = 160$ in Kwon & Choi 1996; 0.185 at $Re = 150$ in Inoue & Yamazaki 1999).

Figure 3(b) also shows that the amplitude of $C_L(\sim 0.52)$ is much larger than that of $C_D(\sim 0.026)$, suggesting that the intensity of a dipole sound associated with the drag force is smaller than that associated with the lift force, in agreement with experiments (for example, Gerrard 1955). Therefore, the Mach number is not expected to seriously affect the generation mechanism of the sound, as far as the Mach number range treated in this study is concerned; in the following discussion on the near-field flow structure and the sound generation, unless otherwise mentioned, we are mainly concerned with the flow at $M = 0.2$.

In order to see the near-field flow structure, forces acting on the cylinder and surface pressure fluctuations are presented in figure 4, and time development of the

https://doi.org/10.1017/S0022112002002124 Published online by Cambridge University Press

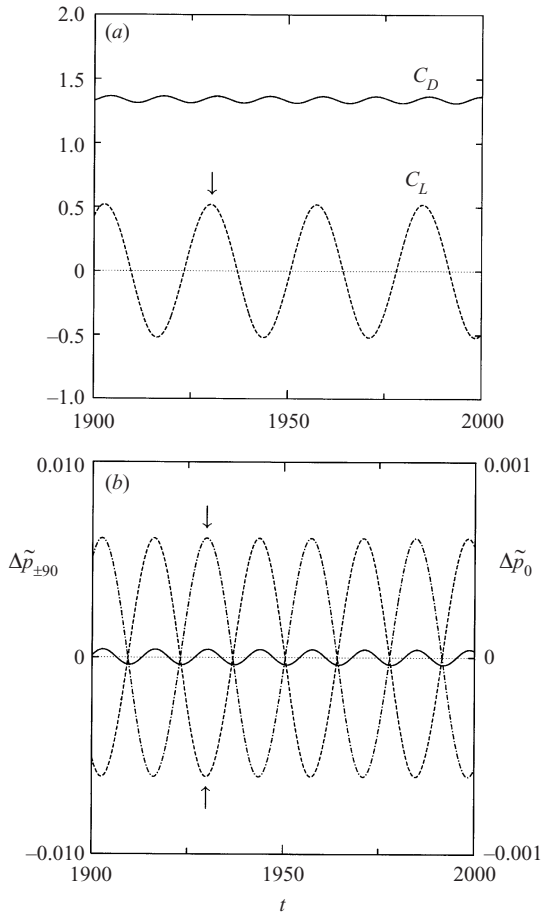


FIGURE 4. Forces acting on the cylinder and fluctuations of the surface pressure. $M = 0.2$, $Re = 150$. Arrows indicate $t = 1930$. (*a*) Lift and drag coefficients: ——, C_D; – – – –, C_L. (*b*) Time-history of the pressure fluctuation $\Delta\tilde{p}$ on the cylinder surface. $r = 0.5$: ——, $\theta = 0°$; – – – –, $\theta = 90°$; – · – · –, $\theta = -90°$.

flow field is shown in terms of vorticity in figure 5 and in terms of fluctuation pressure in figure 6, respectively, for the case of $M = 0.2$. In this case, the Strouhal number St calculated from velocity fluctuations in the wake was about 0.183, and the period of vortex shedding $\Delta T (\equiv St^{-1}M^{-1})$ is $\Delta T \simeq 27.3$. The fluctuation pressure $\Delta\tilde{p}$ is defined by $\Delta\tilde{p}(x, y, t) = \Delta p(x, y, t) - \Delta p_{mean}(x, y)$. Here, Δp denotes the total pressure which is defined by $\Delta p = p - p_\infty$, and Δp_{mean} is the mean pressure; p_∞ denotes the ambient pressure. In figure 4(*b*), $\Delta\tilde{p}_0$ denotes $\Delta\tilde{p}$ at $\theta = 0°$, and $\Delta\tilde{p}_{\pm 90}$ denotes $\Delta\tilde{p}$ at $\theta = \pm 90°$. (For the coordinate system (r, θ), see figure 1.) The scale on the left-hand side is for $\Delta\tilde{p}_{\pm 90}$, and that on the right-hand side is for $\Delta\tilde{p}_0$. As seen from figure 4, the period of C_L is equal to the period of $\Delta\tilde{p}_{\pm 90}$; both equal the period $\Delta T (\simeq 27.3)$ of vortex shedding. The period of C_D is equal to the period of $\Delta\tilde{p}_0$; both equal $\Delta T/2$. Positive peaks of C_L coincide with positive peaks of $\Delta\tilde{p}_{-90}$ and negative peaks of $\Delta\tilde{p}_{+90}$. Similarly, negative peaks of C_L coincide with positive peaks of $\Delta\tilde{p}_{+90}$ and negative peaks of $\Delta\tilde{p}_{-90}$. Maximum values of C_D and $\Delta\tilde{p}_0$ coincide with both of the positive and negative peaks of C_L. On the other hand, minimum values of C_D and $\Delta\tilde{p}_0$ appear at vanishing C_L. Figure 4(*b*) also shows that the amplitude

https://doi.org/10.1017/S0022112002002124 Published online by Cambridge University Press

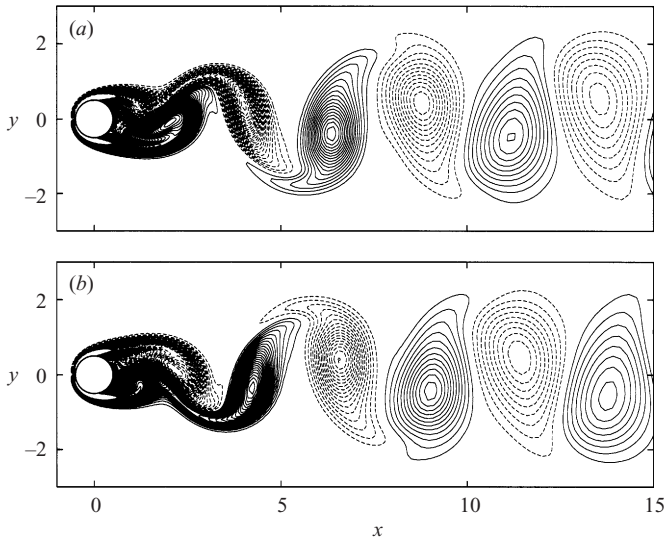


FIGURE 5. Time development of a vorticity field. $M = 0.2$, $Re = 150$. The contour levels are from $\omega_{min} = -1.0$ to $\omega_{max} = 1.0$ with an increment of 0.02: ——, $\omega > 0$; – – – –, $\omega < 0$. (*a*) $t = 1930$, (*b*) $t = 1945$.

of $\Delta\tilde{p}_0$ is much smaller than that of $\Delta\tilde{p}_{\pm 90}$, in agreement with the result shown in figure 4(*a*) that the amplitude of C_L is much larger than that of C_D. As we will see below, the surface pressure fluctuations propagate radially to form sound pressure waves.

We can see from figure 4(*a*) that, during the period $t = 1923$–1937, C_L takes a positive value with its peak at $t = 1930$, which is indicated by arrows. The vorticity field in figure 5 shows that a vortex is shed from the upper side of the cylinder during this period. Similarly, during the period $t = 1937$–1951 when C_L takes a negative value with its peak at $t = 1944$, a vortex is shed from the lower side of the cylinder. Time development of the fluctuation pressure field in figure 6 shows that pressure waves are generated from both upper and lower sides of the cylinder in response to the vortex shedding. For example, as seen from figures 6(*a*) to 6(*d*), during the period $t = 1923$–1937 when a vortex is shed from the upper side of the cylinder, a negative pressure pulse is generated from the upper side of the cylinder and a positive pressure pulse is generated from the lower side of the cylinder; the pulses are denoted by the symbols $\ominus$ and $\oplus$, respectively, in figure 6(*d*). We can see from the figures that the pulses propagate radially with time. Similarly, during the period $t = 1937$–1951 when a vortex is shed from the lower side of the cylinder, a negative pressure pulse is generated from the lower side of the cylinder and a positive pressure pulse is generated from the upper side of the cylinder, as seen from figures 6(*d*) to 6(*g*); the pulses are denoted in figure 6(*g*) by the same symbols as in figure 6(*d*). Therefore, alternate vortex shedding from the upper and lower sides of the cylinder produces positive and negative pressure pulses alternately from both sides of the cylinder, resulting in the generation of pressure waves on both the upper ($y > 0$) and lower ($y < 0$) planes. Figure 6 shows that both positive and negative pressure pulses propagate upstream; the propagation angle θ_p is approximately $\theta_p = 78.5°$. This is due to the Doppler effect, which we will discuss later in more detail in § 3.4.2.

https://doi.org/10.1017/S0022112002002124 Published online by Cambridge University Press

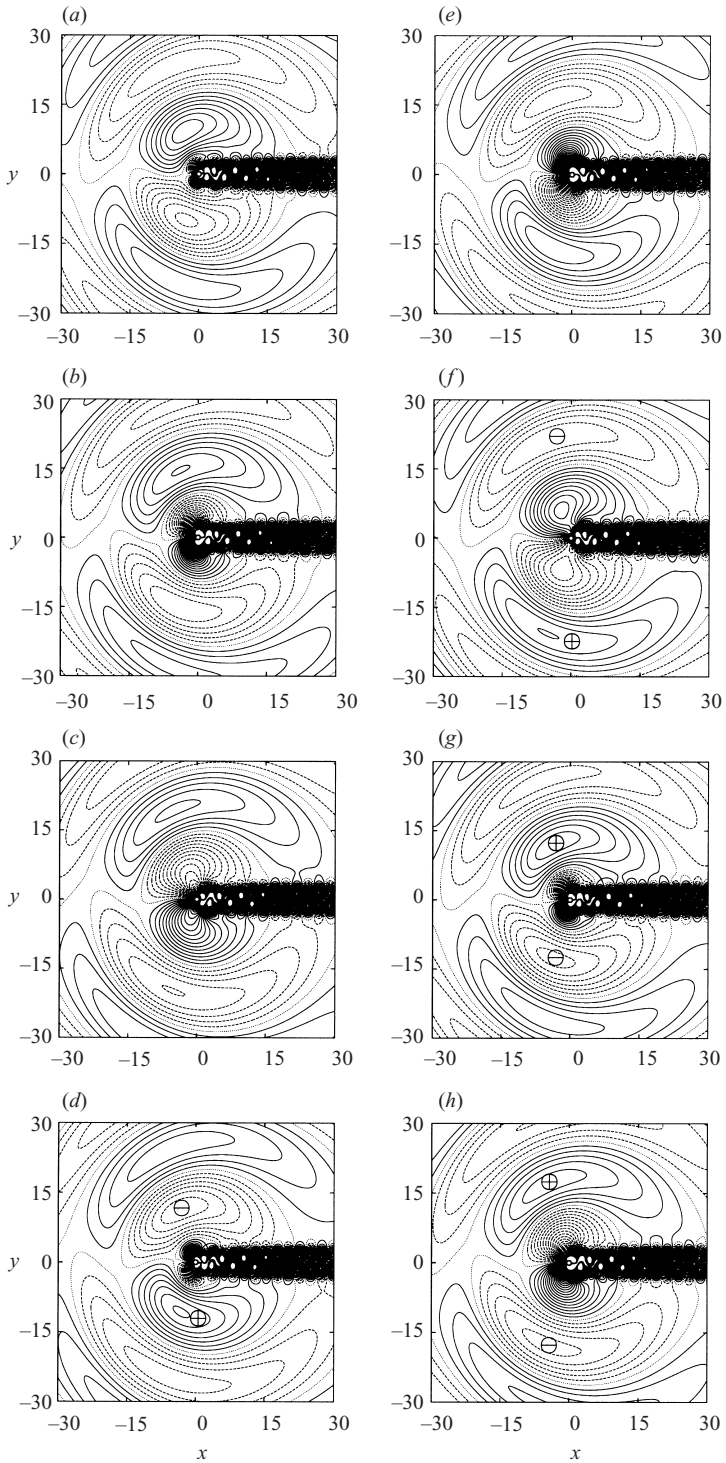


FIGURE 6. Time development of a fluctuation pressure field, $\Delta\tilde{p}$. $M = 0.2$, $Re = 150$. The contour levels are from $\Delta\tilde{p}_{min} = -0.1M^{2.5}$ to $\Delta\tilde{p}_{max} = 0.1M^{2.5}$ with an increment of $0.0025M^{2.5}$. ——, $\Delta\tilde{p} > 0$; – – – –, $\Delta\tilde{p} < 0$. (*a*) $t = 1925$, (*b*) $t = 1930$, (*c*) $t = 1935$, (*d*) $t = 1940$, (*e*) $t = 1945$, (*f*) $t = 1950$, (*g*) $t = 1955$, (*h*) $t = 1960$.

https://doi.org/10.1017/S0022112002002124 Published online by Cambridge University Press

3.2. *Propagation of pressure waves*

In contrast to the generation mechanism of the sound in the near field, the nature of the sound in the intermediate and far fields is affected by the Mach number, as we will see below. This is mainly due to the Doppler effect.

3.2.1. *The effect of the mean pressure*

As shown in the previous section, sound pressure waves are generated in response to vortex shedding, and the generation mechanism of sound pressure waves can be described by the fluctuation pressure $\Delta\tilde{p}(x, y, t)(\equiv \Delta p(x, y, t) - \Delta p_{mean}(x, y))$ which does not include the effect of the mean pressure. Because $\Delta p_{mean}(x, y)$ does not contain temporal information, the propagation process of the pressure waves is also expected to be characterized by the fluctuation pressure. However, before proceeding to the analysis of the propagation mechanism, we should keep in mind the following point concerning the mean pressure.

A typical example of the three pressures over the entire field is presented in figure 7 for $M = 0.2$: figure 7(a) shows the total pressure which includes the effect of the mean pressure, figure 7(b) shows the fluctuation pressure at the same instant as in figure 7(a), and figure 7(c) shows the mean pressure. In figure 7(a), the symbols $\oplus$ and $\ominus$ denote the positive and negative pressure pulses, respectively, which were generated during the period $t = 1923$–1937 and shown in figures 6(d) and 6(f) by the same symbols. The total pressure in figure 7(a) seems to suggest that the positive pressure pulses may propagate upstream whereas the negative pressure pulses may propagate downstream; the propagation angle is $\theta_p \sim \pm 50^\circ$ for the positive pulses and $\theta_p \sim \pm 120^\circ$ for the negative pulses. On the other hand, the fluctuation pressure in figure 7(b) seems to suggest that both positive and negative pulses may propagate upstream; the propagation angle is $\theta_p \sim \pm 78.5^\circ$. Thus, from these plots, it looks as if the propagation angles of the total pressure and the fluctuation pressure are different. Clearly, this is not true because the difference between the total pressure and the fluctuation pressure is the mean pressure which does not contain temporal information.

Figure 8 shows radial distributions of the total pressure Δp (dashed line), the fluctuation pressure $\Delta\tilde{p}$ (solid line) and the mean pressure Δp_{mean} (chain-dotted line). These are measured at three different angles: $\theta = 50^\circ, 78.5^\circ$ and 120°. We can see from figure 8 that the magnitude of the fluctuation pressure is largest at $\theta = 78.5^\circ$, but, because of the mean pressure added to the fluctuation pressure, the positive peaks of the total pressure are largest at $\theta = 50^\circ$ and the negative peaks are largest at $\theta = 120^\circ$. Therefore, in the total pressure field, the pressure waves look as if the positive parts propagate upstream and the negative parts propagate downstream; in fact, the pressure waves propagate upstream (due to the Doppler effect), as clearly shown by the fluctuation pressure. In order to correctly analyse the propagation process, we should look at the fluctuation pressure.

3.2.2. *Decomposition of the sound pressure*

The fluctuation pressure $\Delta\tilde{p}(\equiv \Delta p - \Delta p_{mean})$ can be expressed generally as

$$\begin{aligned}\Delta\tilde{p}(r, \theta, t) = {} & A_0(r, t) \\ & + A_1(r, t)\cos(\theta) + B_1(r, t)\sin(\theta) \\ & + A_2(r, t)\cos(2\theta) + B_2(r, t)\sin(2\theta) \\ & + \cdots,\end{aligned} \tag{3.1}$$

https://doi.org/10.1017/S0022112002002124 Published online by Cambridge University Press

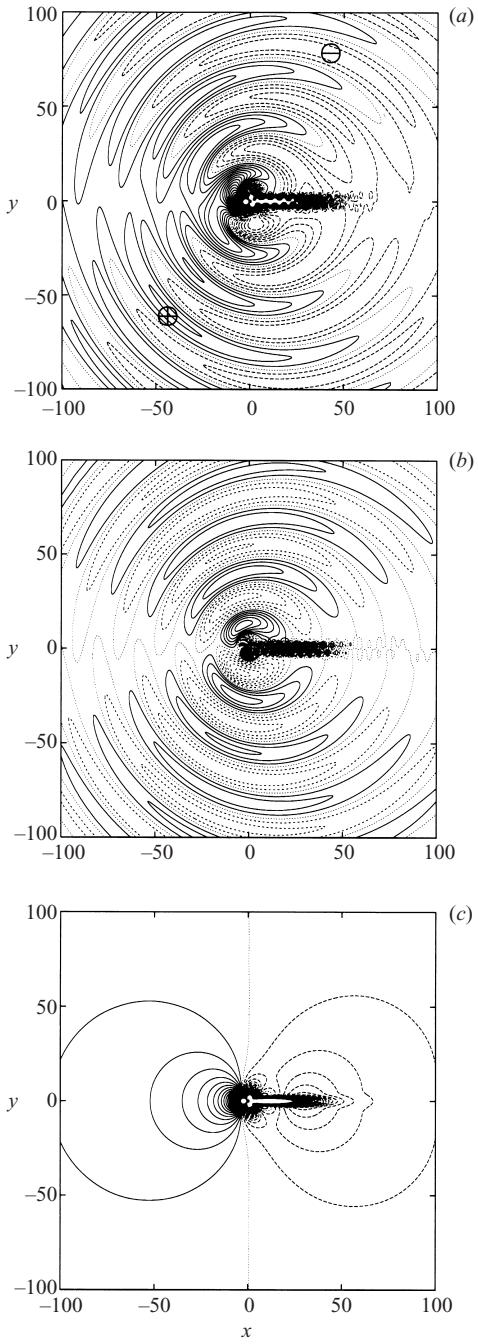


FIGURE 7. Three different views of a pressure field. $M = 0.2$, $Re = 150$. The contour levels are the same as in figure 6; ——, positive pressure; – – – –, negative pressure. (*a*) Total pressure, $\Delta p, t = 2010$, (*b*) fluctuation pressure, $\Delta\tilde{p}, t = 2010$, (*c*) mean pressure, Δp_{mean}.

https://doi.org/10.1017/S0022112002002124 Published online by Cambridge University Press

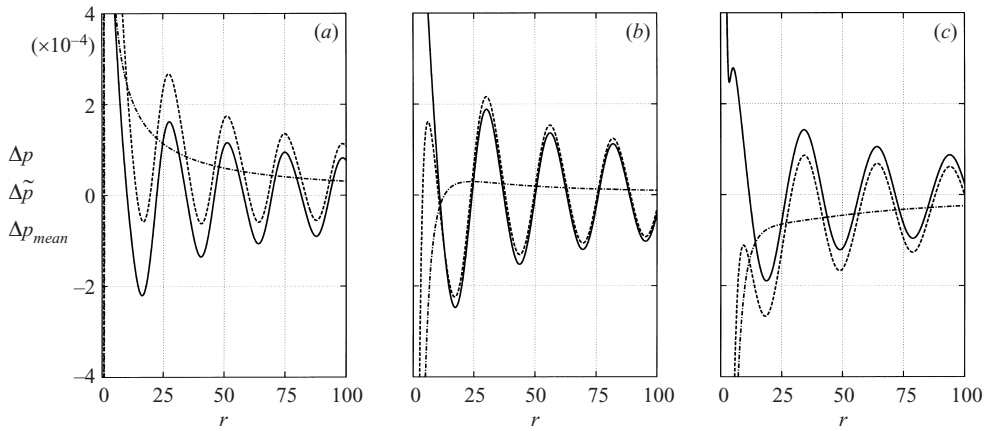


FIGURE 8. Radial distributions of the three pressures. $M = 0.2$, $Re = 150$, $t = 2000$. – – – –, Δp; ——, $\Delta\tilde{p}$; – · – · –, Δp_{mean}. (*a*) $\theta = 50°$, (*b*) $\theta = 78.5°$, (*c*) $\theta = 120°$.

where

$$\left.\begin{aligned} A_0 &= \frac{1}{2\pi}\int_0^{2\pi} \Delta\tilde{p}\,\mathrm{d}\theta, \\ A_n &= \frac{1}{\pi}\int_0^{2\pi} \Delta\tilde{p}\cos(n\theta)\,\mathrm{d}\theta, \\ B_n &= \frac{1}{\pi}\int_0^{2\pi} \Delta\tilde{p}\sin(n\theta)\,\mathrm{d}\theta. \end{aligned}\right\} \tag{3.2}$$

The first term (A_0) of the right-hand side of (3.1) is called the monopole, the second and third terms (A_1, B_1) the dipole, the fourth and fifth terms (A_2, B_2) the quadrupole. The coefficients A_n, B_n are obtained by substituting the present DNS results into $\Delta\tilde{p}$ of (3.2). Shown in figure 9 are the coefficients for three different Mach numbers ($M = 0.1$, 0.2, and 0.3), which were obtained by substituting into (3.2) the DNS results measured at $r = 75$. In the figure, the solid line denotes the fluctuation pressure $\Delta\tilde{p}$ obtained by DNS at $r = 75, \theta = 90°$. The sound generated by a flow past a cylinder is expected to be dominated by dipoles, especially by the lift dipole (Curle 1955; Gerrard 1955; Phillips 1956). As seen from figure 9(*a*), the lift dipole B_1 (chain-dotted line) well-approximates $\Delta\tilde{p}$ (solid line), indicating that indeed the lift dipole dominates the sound field at $M = 0.1$. However, figures 9(*b*) and 9(*c*) show that the deviation of B_1 from $\Delta\tilde{p}$ becomes larger with increased M. As the Mach number is increased, the Doppler effect is expected to play an increasing role, and thus the above deviation of B_1 from $\Delta\tilde{p}$ may possibly be due to the Doppler effect.

3.2.3. *Doppler effect*

In order to examine the Doppler effect acting on the sound field, we introduce a modified fluctuation pressure $\Delta\tilde{p}^M(r', \theta, t)$ by applying the following transformation (Appendix A):

$$\Delta\tilde{p}^M(r', \theta, t) = \sum_{n=0}^{\infty} \Delta\tilde{p}_n^M(r', \theta, t), \tag{3.3}$$

https://doi.org/10.1017/S0022112002002124 Published online by Cambridge University Press

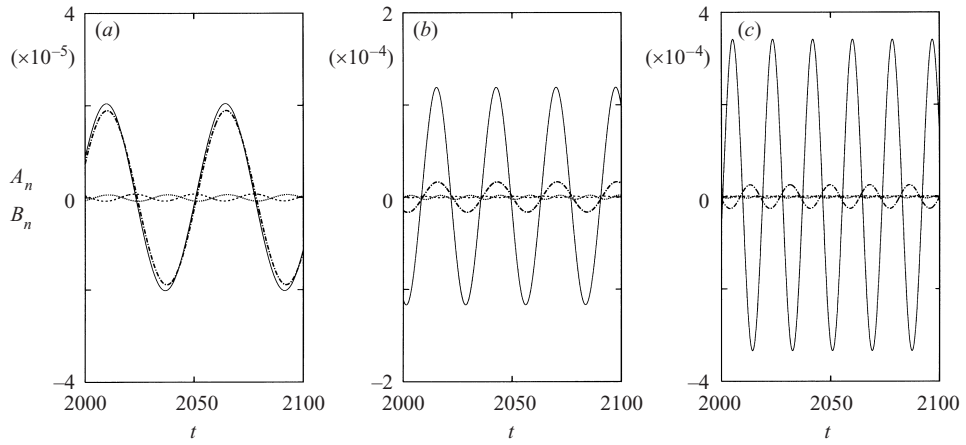


FIGURE 9. Amplitudes of wave modes. Measured at $r = 75$. $Re = 150$. (*a*) $M = 0.1$, (*b*) $M = 0.2$, (*c*) $M = 0.3$. ——, $\Delta\tilde{p}$ (DNS) at $r = 75$, $\theta = 90°$; – – – –, A_0 (monopole); – · – · –, B_1 (dipole); · · · · · ·, $-A_2$ (quadrupole).

$$\Delta\tilde{p}(r,\theta,t) = \sum_{n=0}^{\infty} \Delta\tilde{p}_n^M \left(\frac{r'}{r}\right)^n, \tag{3.4}$$

$$r' = r/(1 - M\cos\theta), \tag{3.5}$$

where $(1 - M\cos\theta)$ is called the Doppler factor (Goldstein 1976). By this transformation, the Doppler effect has been deleted from the fluctuation pressure, and (3.1) and (3.2) are transformed, respectively, to (3.6) and (3.9) as follows:

$$\begin{aligned}\Delta\tilde{p}(r,\theta,t) = {} & A_0'(r',t) \\ & + [A_1'(r',t)\cos(\theta) + B_1'(r',t)\sin(\theta)] \\ & + [A_2'(r',t)\cos(2\theta) + B_2'(r',t)\sin(2\theta)] \\ & + \cdots,\end{aligned} \tag{3.6}$$

where

$$\Delta\tilde{p}_0^M = A_0', \tag{3.7}$$

$$\Delta\tilde{p}_n^M \left(\frac{r'}{r}\right)^n = A_n'\cos(n\theta) + B_n'\sin(n\theta), \tag{3.8}$$

and

$$\left.\begin{aligned} A_0' &= \frac{1}{2\pi}\int_0^{2\pi} \Delta\tilde{p}(r,\theta,t)\,\mathrm{d}\theta, \\ A_n' &= \left(\frac{r'}{r}\right)^n \times \frac{1}{\pi}\int_0^{2\pi} \Delta\tilde{p}(r,\theta,t)\left(\frac{r}{r'}\right)^n \cos(n\theta)\,\mathrm{d}\theta, \\ B_n' &= \left(\frac{r'}{r}\right)^n \times \frac{1}{\pi}\int_0^{2\pi} \Delta\tilde{p}(r,\theta,t)\left(\frac{r}{r'}\right)^n \sin(n\theta)\,\mathrm{d}\theta. \end{aligned}\right\} \tag{3.9}$$

Shown in figure 10 are the transformed coefficients A_n', B_n' obtained from (3.9) for the same flow conditions as in figure 9. As readily seen from figure 10, the lift dipole (B_1', chain-dotted line) now almost completely overlaps the DNS fluctuation pressure $\Delta\tilde{p}$ (solid line), irrespective of M, indicating that the lift dipole dominates the sound field.

https://doi.org/10.1017/S0022112002002124 Published online by Cambridge University Press

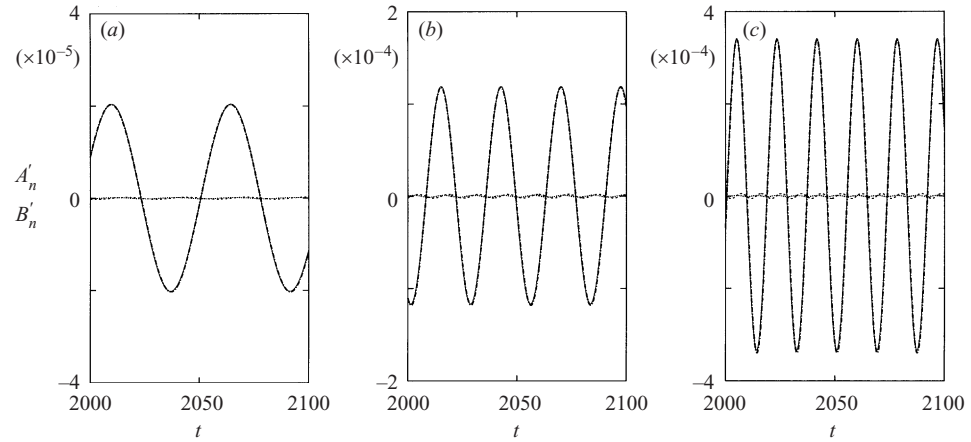


FIGURE 10. Modified amplitudes of wave modes in which the Doppler effect has been removed. Measured at $r' = 75$. $Re = 150$. (*a*) $M = 0.1$, (*b*) $M = 0.2$, (*c*) $M = 0.3$. ——, $\Delta\tilde{p}$ (DNS) at $r = r'(1 - M\cos\theta)$ with $r' = 75, \theta = 90°$; – – – –, A'_0 (monopole); –·–·–, B'_1 (dipole); ·····, $-A'_2$ (quadrupole).

This result together with that shown in figure 9 clearly demonstrates the importance of the Doppler effect at finite Mach numbers.

3.2.4. *Directivity of the pressure waves*

In an experiment on head-on collision of two vortex rings, Minota & Kambe (1986) obtained a time sequence of the polar diagram of the pressure, and demonstrated the quadrupolar nature of the generated sound by showing the four-lobe curves. Inoue *et al.* (2000) computationally obtained a time sequence of the polar diagram of the pressure for the same problem which reproduced the four-lobe curves observed by Minota & Kambe. The same method as that used in Inoue *et al.* was applied to the present problem in order to show the directivity of the pressure waves.

As shown in figure 10, the sound field is dominated by the lift dipole; the fluctuation pressure $\Delta\tilde{p}$ is closely approximated by the dipole term $\Delta\tilde{p}_1^M(r'/r)$ in (3.4). Taking this result into account, we consider the following approximation:

$$\Delta\tilde{p}^M(r', \theta, t) = \left(\frac{r}{r'}\right)\Delta\tilde{p}(r, \theta, t) \tag{3.10}$$

Hereafter, the symbol $\Delta\tilde{p}^M$ denotes the modified fluctuation pressure defined by (3.10), instead of (3.3) and (3.4). Figure 11 shows polar diagrams of the modified fluctuation pressure $\Delta\tilde{p}^M$, defined by (3.10), measured at $r' = 75$ for the case of $M = 0.2$. In each diagram, the radial length from the origin represents the magnitude of the pressure on a linear scale with the outermost circle being $|\Delta\tilde{p}| = 2 \times 10^{-4}$. The symbols • and ○ denote positive and negative values of the pressure, respectively. If we assume that the pressure waves propagate at the speed of sound, it takes about 74.5 non-dimensional time units for the waves which were generated near the cylinder surface ($r = 0.5$) to arrive at $r' = 75$. Therefore, the polar diagrams in figure 11 may be considered to show the directivity of the pressure waves generated by the vortex shedding during the period $t = 1925$–1945 (see also figures 4 and 5). Figure 11(*b*) corresponds to a maximum C_L at $t \approx 1930$ in figure 4(*a*). Similarly, figure 11(*d*) corresponds to a mimimum C_L, and figures 11(*a*) and 11(*c*) correspond to vanishing C_L. From figure 11, we can readily see that the sound field is dominated by the lift dipole: the profile

https://doi.org/10.1017/S0022112002002124 Published online by Cambridge University Press

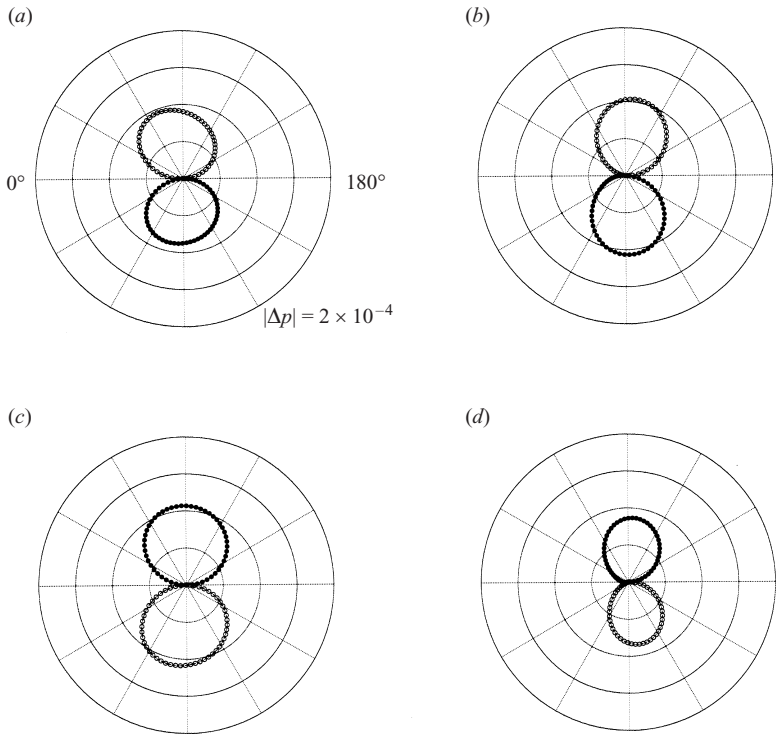


FIGURE 11. Time variation of a polar diagram of the modified fluctuation pressure, $\Delta\tilde{p}^M$. $M = 0.2$, $Re = 150$. Measured at $r' = 75$. ●, $\Delta\tilde{p}^M > 0$; ○, $\Delta\tilde{p}^M < 0$. (*a*) $t = 2000$, (*b*) $t = 2005$, (*c*) $t = 2015$, (*d*) $t = 2020$.

is approximately symmetric and the signs of the pressure are opposite with respect to lines $\theta = 0°$ and 180°. The directivity fluctuates around $\theta = \pm 90°$ at the same frequency as the vortex shedding frequency, because it is affected not only by the lift dipole but also by the drag dipole which is generated at $\theta = 0°$.

Shown in figure 12 are the polar plots of the root mean square of the fluctuation pressures, $\Delta\tilde{p}$ (figure 12*a*) and $\Delta\tilde{p}^M$ (figure 12*b*). Both figures show the dipolar nature of the sound field. Note that the root mean square of $\Delta\tilde{p}$ in figure 12(*a*) shows the directivity at $\theta \approx 78.5°$, while that of $\Delta\tilde{p}^M$ in figure 12(*b*) shows the directivity at $\theta \approx 90°$. This difference is due to the Doppler effect. We will discuss this point later in more detail in § 3.4.2.

3.2.5. *Decay of the sound pressure*

Instantaneous distributions of the fluctuation pressure $\Delta\tilde{p}$ are presented against the distance r in figure 13(*a*) at $\theta = 90°$. Different lines denote different times. As seen from figure 13(*a*), pressure waves propagate radially with time. Owing to the Doppler effect, the propagation velocity of the waves is dependent on the angle θ and is described by $c_\theta(\theta) = c_\infty(1 - M\cos\theta)$; it is equal to the speed of sound c_∞ at $\theta = 90°$, which can be confirmed in figure 13(*a*). Figure 13(*a*) also shows that peak values of the pressure decay with increasing distance r. Plotted in figure 13(*b*) are the peak values of the fluctuation pressure against r at $\theta = 90°$. As is readily seen from figure 13(*b*), the pressure peaks tend to decay in proportion to $r^{-1/2}$ with increasing r, in agreement with the theoretical prediction (Landau & Lifshitz 1987).

https://doi.org/10.1017/S0022112002002124 Published online by Cambridge University Press

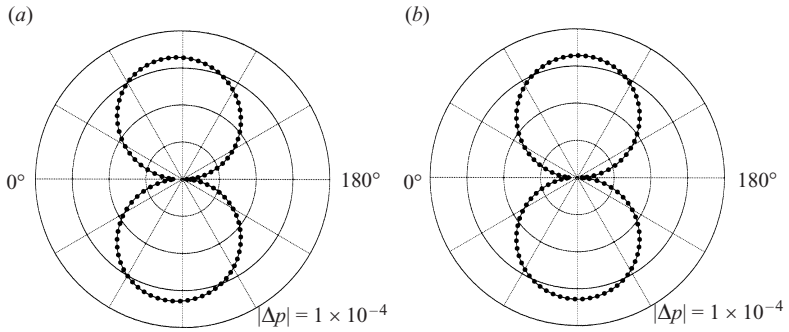


FIGURE 12. Polar plots of the root mean square of the fluctuation pressures. $M = 0.2$, $Re = 150$. (*a*) $\Delta\tilde{p}$ at $r = r'(1 - M\cos\theta)$ with $r' = 75$, (*b*) $\Delta\tilde{p}^M$ at $r' = 75$.

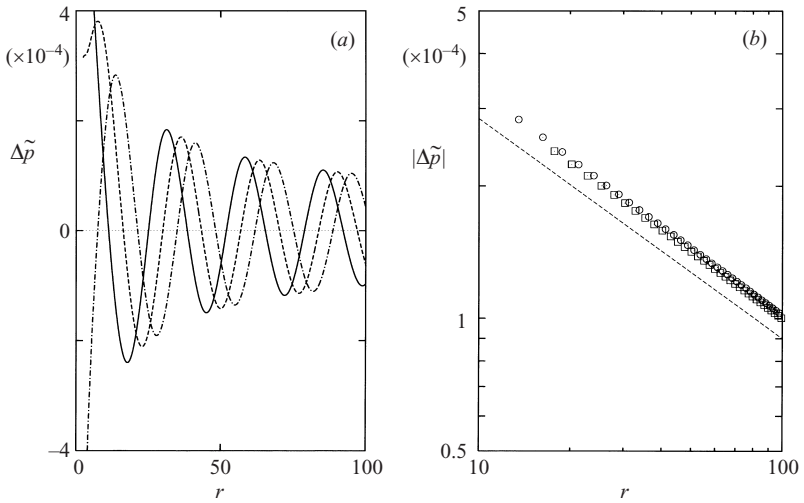


FIGURE 13. Propagation and decay of pressure waves. $M = 0.2$, $Re = 150$. $\theta = 90°$. (*a*) Propagation of pressure waves $\Delta\tilde{p}$. ——, $t = 2000$; – – – –, $t = 2005$; – · – · –, $t = 2010$. (*b*) Decay of pressure peaks. ○, $\Delta\tilde{p} > 0$; □, $\Delta\tilde{p} < 0$; – – – –, $\propto r^{-1/2}$.

3.3. *Far-field nature of the sound and scaling law*

Curle (1955) extended Lighthill's acoustic analogy (Lighthill 1952) to include the influence of solid boundaries on the sound field. The two-dimensional form of Curle's exact solution may be expressed in a dimensional form as (Appendix B)

$$c_\infty^2[\rho(\boldsymbol{x}', t) - \rho_\infty] = \frac{\partial^2}{\partial x_i' \partial x_j'} \int_V \mathrm{d}\boldsymbol{y}' \int_{-\infty}^{t-|\boldsymbol{x}'-\boldsymbol{y}'|/c_\infty} \frac{T_{ij}(\boldsymbol{y}', t')\,\mathrm{d}t'}{2\pi\sqrt{(t-t')^2 - |\boldsymbol{x}'-\boldsymbol{y}'|^2/c_\infty^2}}$$
$$- \frac{\partial}{\partial x_i'} \oint_S \mathrm{d}\ell(\boldsymbol{y}') \int_{-\infty}^{t-|\boldsymbol{x}'-\boldsymbol{y}'|/c_\infty} \frac{f_i(\boldsymbol{y}', t')\,\mathrm{d}t'}{2\pi\sqrt{(t-t')^2 - |\boldsymbol{x}'-\boldsymbol{y}'|^2/c_\infty^2}}, \tag{3.11}$$

where

$$T_{ij} = \rho u_i u_j + \delta_{ij}[(p - p_\infty) - c_\infty^2(\rho - \rho_\infty)] - e_{ij} \tag{3.12}$$

is Lighthill's stress tensor. The symbol ρ denotes the density, δ_{ij} the Kronecker delta and e_{ij} the viscous part of the Stokes stress tensor; f_i is the force per unit length

https://doi.org/10.1017/S0022112002002124 Published online by Cambridge University Press

exerted on the fluid by the solid boundaries in the i-direction. Because in Curle's analogy the flow in the far field is assumed to be stationary and thus the Doppler effect is not taken into consideration, the coordinate system is given by $\boldsymbol{x}'$ or r', instead of $\boldsymbol{x}$ or r. The first term of the right-hand side of (3.11) is equivalent to the sound generated by a volume distribution of quadrupoles. The second term represents the influence of the solid boundaries and is equivalent to the sound generated by a surface distribution of dipoles of strength f_i. A similar expression to (3.11) can be seen in Ffowcs Williams (1969), where the second term of the right-hand side is not included. If we assume that the source region is compact and the flow is isentropic, $p - p_\infty = c_\infty^2(\rho - \rho_\infty)$, then (3.11) may be reduced to

$$p(\boldsymbol{x}', t) - p_\infty = \frac{x_i' x_j'}{2^{3/2}\pi c_\infty^{3/2}|\boldsymbol{x}'|^{5/2}} \int_{-\infty}^{\tau} \left[\frac{\partial^2}{\partial t'^2} \int_V T_{ij}(\boldsymbol{y}', t')\, \mathrm{d}\boldsymbol{y}' \right] \frac{\mathrm{d}t'}{\sqrt{\tau - t'}} + \frac{x_i'}{2^{3/2}\pi c_\infty^{1/2}|\boldsymbol{x}'|^{3/2}} \int_{-\infty}^{\tau} \left[\frac{\partial}{\partial t'} \oint_S f_i(\boldsymbol{y}', t')\, \mathrm{d}\ell(\boldsymbol{y}') \right] \frac{\mathrm{d}t'}{\sqrt{\tau - t'}}, \quad (3.13)$$

where $\tau = t - |\boldsymbol{x}'|/c_\infty$ is the retarded time. A similar expression to (3.13) can be found in Howe (1998), where the second term of the right-hand side is not included. It should be noted here that, in the reduction process from (3.11) to (3.13), the space derivatives $\partial/\partial x_i'$, $\partial^2/\partial x_i'\partial x_j'$ of the right-hand side of (3.11) were replaced with the time derivatives $\partial/\partial t'$, $\partial^2/\partial t'^2$, under the assumption of compact flow; the effect of mean pressure field is excluded in this process and thus is not included in (3.13). Therefore, the pressure in the left-hand side of (3.13) should be interpreted as the fluctuation pressure ($\Delta\tilde{p} \equiv \Delta p - \Delta p_{mean}$), though it is conventionally considered as the total pressure ($\Delta p \equiv p - p_\infty$ in the present notation).

The two terms of the right-hand side of (3.13) are described by the near-field quantities under the assumption of a compact source. Therefore, if the lengths are normalized by D and the velocity by U_∞, then T_{ij} and f_i are scaled by $\rho_\infty U_\infty^2$ and the time is scaled by D/U_∞. In this case, the magnitude of the first term of the right-hand side of (3.13) is estimated to be $(r/D)^{-1/2}(U_\infty/c_\infty)^{7/2}\rho_\infty c_\infty^2$, and that of the second term to be $(r/D)^{-1/2}(U_\infty/c_\infty)^{5/2}\rho_\infty c_\infty^2$. (The pressure on the left-hand side should not be scaled by U_∞, because it contains the sound pressure which propagates at the speed of sound.) These estimations lead to the following relation in a non-dimensional form:

$$\Delta\tilde{p} \propto (AM^{7/2} + M^{5/2})/r^{1/2}, \quad (3.14)$$

where A is a constant. At sufficiently low Mach numbers, the first term of (3.14) may be neglected and the following scaling law may hold on a time scale of $D/U_\infty (\equiv Mt)$:

$$\Delta\tilde{p} \propto M^{2.5}/r^{1/2}. \quad (3.15)$$

A similar way of estimation had been used by Kambe & Minota (1983) to obtain the scaling law, $\Delta p \propto M^4/r$, for the sound pressure generated by the head-on collision of two vortex rings.

In order to confirm the validity of the scaling law (3.15), the computational results at three different Mach numbers ($M = 0.3$, 0.2, 0.1) are presented in figure 14(a), where the normalized sound pressure, $\Delta\tilde{p}/M^{2.5}$, is plotted against the reduced time $M(t - t_1)$. The symbol t_1 denotes the arrival time of a sound pressure peak at a measurement point; $r = 100, \theta = 90°$. As seen from figure 14(a), coincidence of the curves $\Delta\tilde{p}/M^{2.5}$ versus the reduced time $M(t - t_1)$ is quite good for the Mach number range treated in this paper, supporting the validity of the scaling law. Plotted in

https://doi.org/10.1017/S0022112002002124 Published online by Cambridge University Press

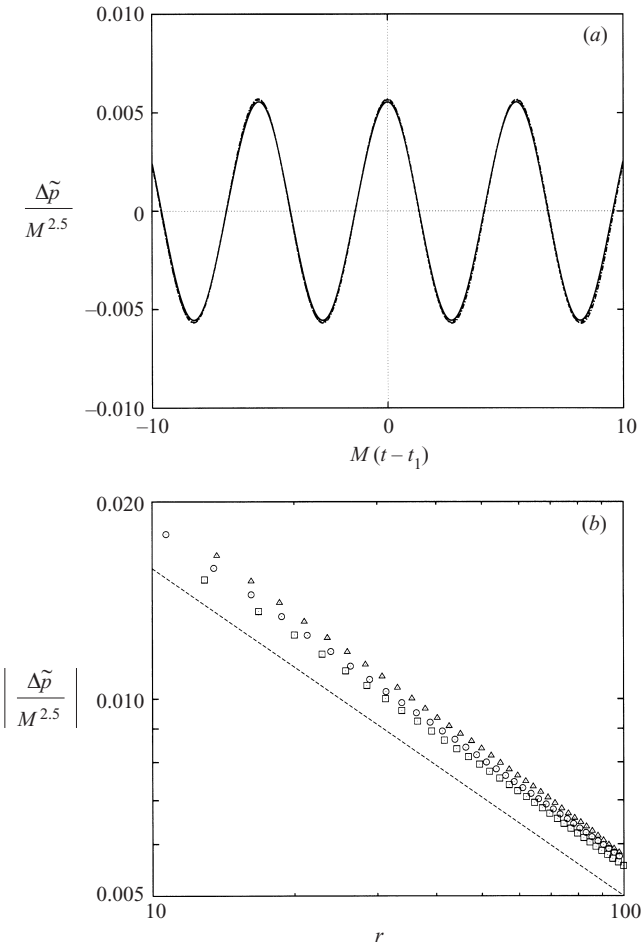


FIGURE 14. Scaling law. $Re = 150$. (a) Time-histories of the normalized pressure, $\Delta\tilde{p}/M^{2.5}$, measured at $r = 100$, $\theta = 90°$. t_1 denotes the arrival time of a pressure peak at the measurement point. –·–·–, $M = 0.3$; – – – –, $M = 0.2$; ——, $M = 0.1$. (b) Decay of the sound pressure, $\Delta\tilde{p}/M^{2.5}$, measured at $\theta = 90°$. △, $M = 0.3$; ○, $M = 0.2$; □, $M = 0.1$.

figure 14(b) is the decay of the pressure peaks, measured at $\theta = 90°$, at the three Mach numbers. The figure clearly shows the decay of $\Delta\tilde{p}/M^{2.5}$ proportional to $r^{-1/2}$.

3.4. *Comparison with Curle's solution*

The most important results in this section are presented in figures 15 and 16 for $M = 0.2$. The left-hand column in figure 15 shows the direct numerical solutions: figure 15(a) shows the total pressure Δp, figure 15(b) shows the fluctuation pressure $\Delta\tilde{p}(\equiv \Delta p - \Delta p_{mean})$, and figure 15($c$) shows the modified fluctuation pressure $\Delta\tilde{p}^M$ in which the Doppler effect has been removed from $\Delta\tilde{p}$. The right-hand column shows the pressures obtained by Curle's acoustic analogy: figure 15(f) shows Curle's solution $\Delta\tilde{p}_{curle}$ in which neither the effect of the mean pressure nor the Doppler effect are included, figure 15(e) shows Curle's modified solution $\Delta\tilde{p}^D_{curle}$ which contains the Doppler effect only, and figure 15(d) shows Curle's modified solution superimposed on the mean pressure, $\Delta\tilde{p}^D_{curle} + \Delta p_{mean}$. It should be noted that the three pressures of the left-hand column are quite similar to those of the right-hand column.

https://doi.org/10.1017/S0022112002002124 Published online by Cambridge University Press

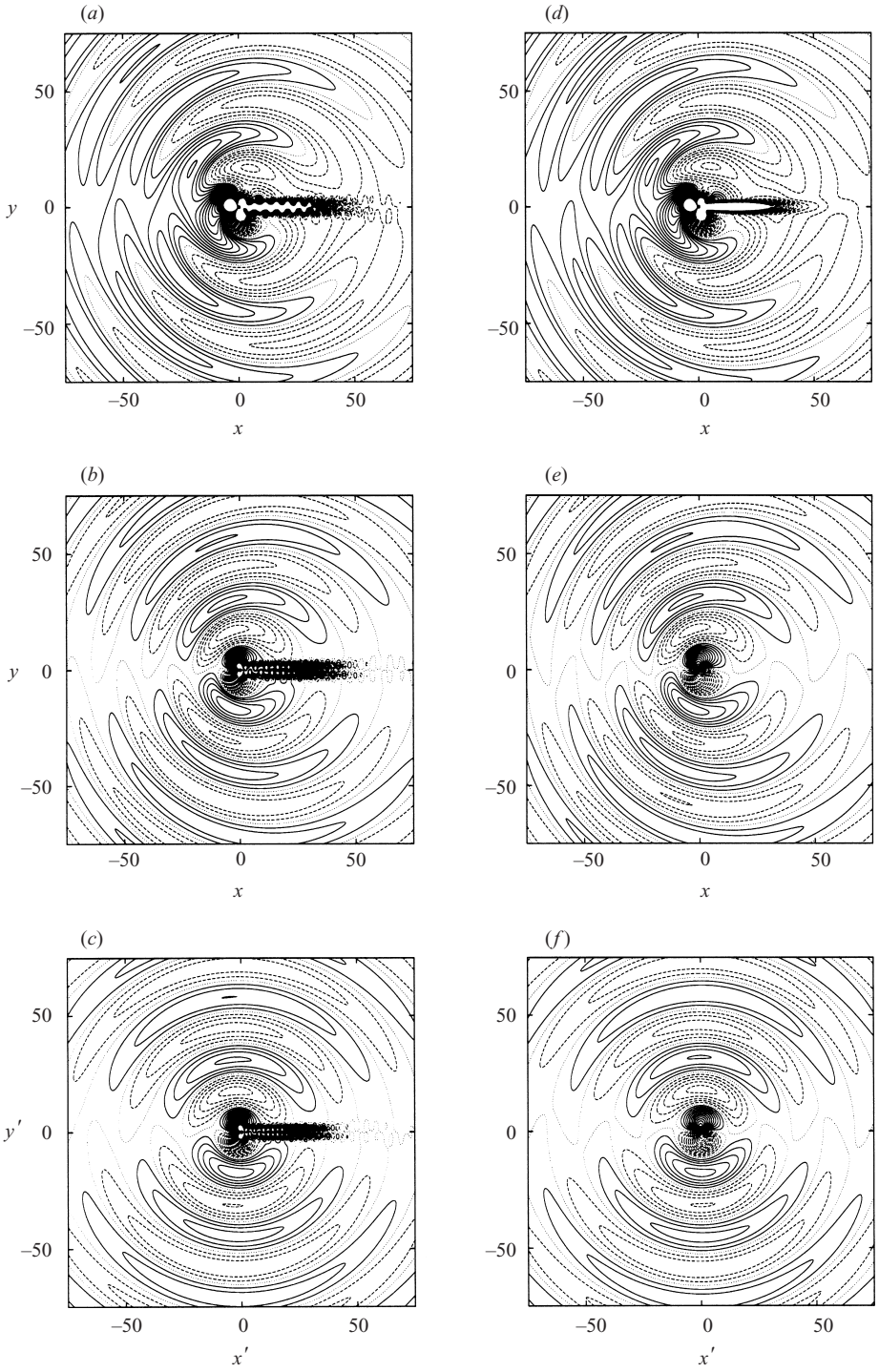


FIGURE 15. Comparison of pressure distributions between DNS and Curle's solutions. $M = 0.2$, $Re = 150$, $t = 2000$. The contour levels are from $-0.1M^{2.5}$ to $0.1M^{2.5}$ with an increment of $0.0025M^{2.5}$. ——, positive pressure; – – – –, negative pressure. (*a*) Δp (DNS), (*b*) $\Delta\tilde{p}$ (DNS), (*c*) $\Delta\tilde{p}^{M}$ (DNS), (*d*) $\Delta\tilde{p}^{D}_{curle} + \Delta p_{mean}$, (*e*) $\Delta\tilde{p}^{D}_{curle}$, (*f*) $\Delta\tilde{p}_{curle}$.

https://doi.org/10.1017/S0022112002002124 Published online by Cambridge University Press

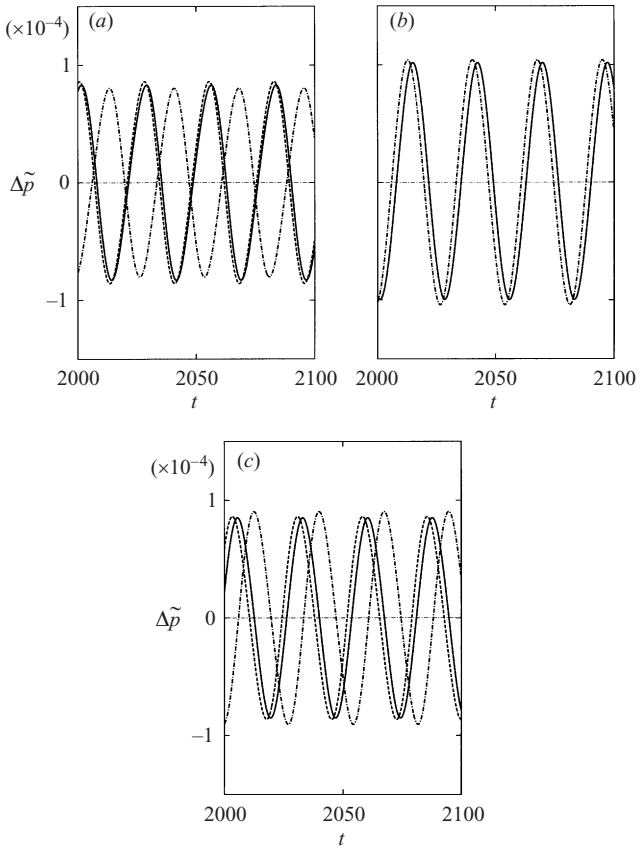


FIGURE 16. Time-histories of the pressure $\Delta\tilde{p}$. $M = 0.2$, $Re = 150$, $t = 2000$. (a) $\theta = 50°$, (b) $\theta = 90°$, (c) $\theta = 120°$. ——, $\Delta\tilde{p}$ (DNS) at $r = 100$; – – – –, $\Delta\tilde{p}^{D}_{curle}$ at $r = 100$; – · – · –, $\Delta\tilde{p}_{curle}$ at $r' = 100$.

Figure 16 shows time histories of the three different pressures: $\Delta\tilde{p}$ (DNS, solid line), $\Delta\tilde{p}_{curle}$ (chain-dotted line), and $\Delta\tilde{p}^{D}_{curle}$ (dashed line). They were measured at three different angles ($\theta = 50°, 90°, 120°$), with a fixed value of $r = 100$ for $\Delta\tilde{p}$ and $\Delta\tilde{p}^{D}_{curle}$ and $r' = 100$ for $\Delta\tilde{p}_{curle}$. Figure 16 shows that Curle's solution $\Delta\tilde{p}_{curle}$ differs from the DNS result in the phase of the pressure waves. Curle's modified solution $\Delta\tilde{p}^{D}_{curle}$ gives a very good agreement with the DNS fluctuation pressure.

In the following subsections, we discuss Curle's acoustic analogy in detail, and try to clarify what figures 15 and 16 mean.

3.4.1. *Curle's acoustic analogy*

As mentioned in the previous section, the magnitude of the second term of (3.14) is of $O(M^{-1})$ compared to the first term. At sufficiently low Mach numbers, therefore, the first term may be neglected and Curle's solution (3.13) may be rewritten as

$$\Delta\tilde{p}_{curle}(\boldsymbol{x}', t) = \frac{1}{2^{3/2}\pi c_\infty^{1/2} r'^{1/2}} \int_{-\infty}^{\tau} \frac{F'(\tau')}{\sqrt{\tau - \tau'}}\, \mathrm{d}\tau',$$

$$r' = |\boldsymbol{x}'|, \quad \tau = t - r'/c_\infty, \quad F'(\tau') = \frac{\partial}{\partial \tau'}\left[\frac{x_i'}{r'} F_i(\tau')\right], \tag{3.16}$$

https://doi.org/10.1017/S0022112002002124 Published online by Cambridge University Press

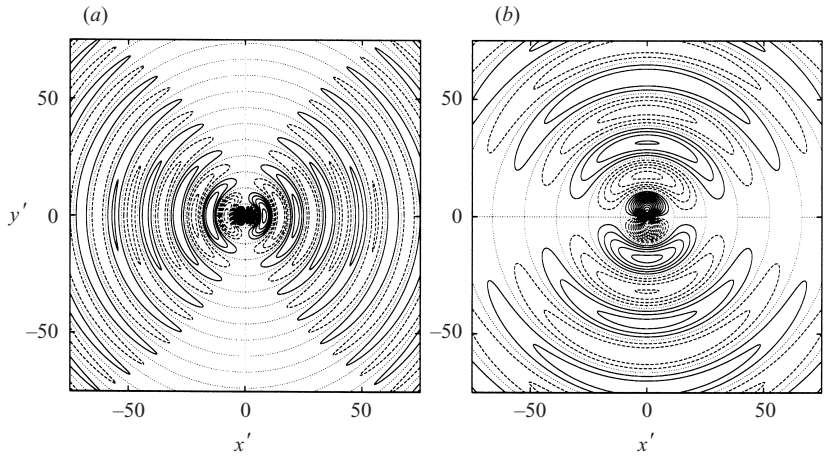


FIGURE 17. Decomposition of the pressure field obtained by Curle's method, $\Delta\tilde{p}_{curle}$. $M = 0.2$, $Re = 150$, $t = 2000$. (*a*) $\Delta\tilde{p}_{curle}$ produced by the drag force, F_x in (3.16), (*b*) $\Delta\tilde{p}_{curle}$ produced by the lift force, F_y in (3.16). The contour levels are from $-0.005 \times M^{2.5}$ to $0.005 \times M^{2.5}$ with an increment of $0.00025 \times M^{2.5}$ for (*a*), and from $-0.05 \times M^{2.5}$ to $0.05 \times M^{2.5}$ with an increment of $0.0025 \times M^{2.5}$ for (*b*). Solid lines denote positive values, and dashed lines denote negative values.

where $F_i = \oint_S f_i(\boldsymbol{y}', t)\,\mathrm{d}\ell$. Figure 15(*f*) shows an instantaneous pressure field, which was obtained from Curle's solution (3.16) by substituting the DNS result into the source term F_i. The solid lines denote positive values of the pressure, and the dashed lines denote negative values. As seen from figure 15(*f*), the result obtained by Curle's solution (3.16) shows that pressure waves propagate at right angles to the flow direction, indicating the dominant effect of the lift dipole. Presented in figures 17(*a*) and 17(*b*) are the pressure fields produced by the drag and lift forces, respectively. Superposition of the two fields gives figure 15(*f*). Note that the contour levels in figure 17(*a*) are much smaller than those in figure 17(*b*). Figure 17 shows that the pressure fluctuation propagating at $\theta = 0^\circ$ is produced by the drag force whereas that propagating at $\theta = 90^\circ$ is produced by the lift force, and that the sound field shown in figure 15(*f*) is indeed dominated by the lift dipole. The pressure field in figure 15(*f*) is different from the DNS result in figures 15(*a*) and 15(*b*) but is quite similar to that shown in figure 15(*c*) which presents the modified fluctuation pressure which does not include the Doppler effect.

Figure 16 shows that Curle's solutions (chain-dotted lines) differ from the DNS results (solid lines) in the phase of the pressure waves. This is especially true for $\theta = 50^\circ$ and 120°.

3.4.2. *Doppler effect*

As already noted in § 3.2, the Doppler effect may play an important role in the propagation process of sound. Therefore, it is possible that the above-mentioned differences in figures 15 and 16 between Curle's solution and the DNS result may be due to the Doppler effect, at least partly. Based on this speculation, we consider the following transformation. From a simple consideration (figure 18), we can see that the propagation speed $c_\theta(\theta)$ of the pressure waves under the Doppler effect may be expressed by

$$c_\theta(\theta) = c_\infty(\sqrt{1 - M^2 \sin^2\theta} - M\cos\theta). \tag{3.17}$$

https://doi.org/10.1017/S0022112002002124 Published online by Cambridge University Press

At sufficiently small Mach numbers, (3.17) may be reduced to

$$c_\theta(\theta) = c_\infty(1 - M\cos\theta). \tag{3.18}$$

By applying (3.18) (together with (A8) for $n = 1$ in Appendix A) to Curle's solution (3.16), we obtain the following expression for Curle's solution which contains the Doppler effect:

$$\Delta\tilde{p}^D_{curle}(\boldsymbol{x}, t) = \frac{1}{2^{3/2}\pi c_\theta^{1/2} r^{1/2}} \int_{-\infty}^{\tau} \frac{F'(\tau')}{\sqrt{\tau - \tau'}}\,\mathrm{d}\tau', \tag{3.19}$$

where the retarded time is now $\tau = t - r/c_\theta$, and the superscript D denotes Curle's solution modified by the transformation (3.18). The resulting pressure field is presented in figure 15(e). As seen from the figure, both positive and negative pressure pulses (or pressure waves) now propagate upstream; quite good agreement is obtained with the fluctuation pressure $\Delta\tilde{p}$ shown in figure 15(b). The propagation angle θ_p of the pulses (or, more precisely, the propagation angle of pressure peaks) may be estimated from (3.19) as follows. The position r of a pulse propagating under the Doppler effect may be written as $r = c_\theta(t - t_0) = r_{90}(1 - M\cos\theta)$, where $t - t_0 = r_{90}/c_\infty$ and t_0 is the generation time of the pulse and r_{90} is r at $\theta = 90°$. Then, the pressure $\Delta\tilde{p}^D_{pulse}$ at r may be written as

$$\begin{aligned}\Delta\tilde{p}^D_{pulse} &= \frac{1}{2^{3/2}\pi c_\theta^{1/2} r^{1/2}} \int_{-\infty}^{\tau} \frac{F'(\tau')}{\sqrt{\tau - \tau'}}\,\mathrm{d}\tau', \\ &= \frac{1}{2^{3/2}\pi(1 - M\cos\theta) c_\infty^{1/2} r_{90}^{1/2}} \int_{-\infty}^{\tau} \frac{F'(\tau')}{\sqrt{\tau - \tau'}}\,\mathrm{d}\tau'.\end{aligned} \tag{3.20}$$

From (3.20), the dependence of $\Delta\tilde{p}^D_{pulse}$ on θ may be described by

$$\Delta\tilde{p}^D_{pulse}(\theta) \propto \frac{F'}{1 - M\cos\theta}, \tag{3.21}$$

where $F' = F'_x\cos\theta + F'_y\sin\theta$. As shown in figure 4, the fluctuation in lift is much larger than that in drag; we may neglect the F'_x term. Therefore, we may assume that $F' \propto \sin\theta$ as a first approximation. In this case, from $(\partial/\partial\theta)[\Delta\tilde{p}^D_{pulse}] = 0$, we can easily obtain the following relation between θ_p and M:

$$\cos\theta_p = M \quad \text{or} \quad \theta_p = \cos^{-1} M. \tag{3.22}$$

For $M = 0.2$, the propagation angle is given by $\theta_p = \pm 78.5°$, which is close to the propagation angle of the pulses in figures 15(b) and 15(e).

In figure 16, Curle's modified solution $\Delta\tilde{p}^D_{curle}$ is presented by dashed lines. We can see from figure 16 that the agreement of the phase between the DNS and Curle's modified solution is very good. As seen from (3.18), due to the Doppler effect the propagation speed $c_\theta(\theta)$ is smaller than c_∞ in the upstream region ($|\theta| < 90°$) while it is larger in the downstream region ($90° < |\theta| < 180°$); it takes more time for the pressure signals to arrive at the measurement point ($r = 100$ in figure 16) in the upstream region than in the downstream region. Therefore, we can see that the phase difference between $\Delta\tilde{p}_{curle}$ and $\Delta\tilde{p}$ (or $\Delta\tilde{p}^D_{curle}$) in figure 16($a$) at $\theta = 50°$ and in figure 16(c) at $\theta = 120°$ is due to the Doppler effect. It should be noticed in figure 16(b), however, that there is a small phase difference between $\Delta\tilde{p}$ and $\Delta\tilde{p}^D_{curle}$ at $\theta = 90°$ where, according to (3.18), the Doppler effect may be vanishing. (In figure 16(b), $\Delta\tilde{p}^D_{curle}$ is not presented because $\Delta\tilde{p}^D_{curle}$ is completely overlapped by $\Delta\tilde{p}_{curle}$ due to the vanishing

https://doi.org/10.1017/S0022112002002124 Published online by Cambridge University Press

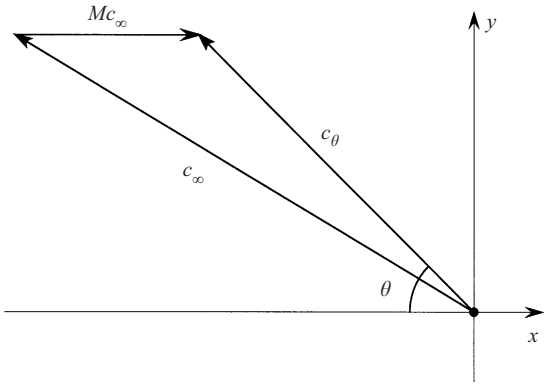


FIGURE 18. Relation between the speed of sound c_∞ and the propagation speed $c_\theta(\theta)$ of pressure waves under the Doppler effect.

Doppler effect at $\theta = 90°$.) The difference is due to the higher-order term, $M^2 \sin^2\theta$ in (3.17), which is neglected in (3.18). Similar differences between $\Delta\tilde{p}$ and $\Delta\tilde{p}^D_{curle}$ are also seen in figures 16(a) and 16(c).

The difference in amplitude observed in figures 15 and 16 between the DNS fluctuation pressure, $\Delta\tilde{p}$, and Curle's modified solution, $\Delta\tilde{p}^D_{curle}$, may be attributed to the sound generated by a volume distribution of quadrupoles, i.e. the first term of the right-hand side of (3.13), which is neglected in Curle's solution $\Delta\tilde{p}^D_{curle}$.

Finally, by comparing figure 15(d) with figure 15(a), we can readily see that agreement of the two figures is very good, except for the wake region where the Kármán vortex street exists. Thus, we may say that in fact Curle's solution (3.16), or its original form (3.13), does not contain the mean pressure, and that by adding it Curle's modified solution (3.19) gives a very good approximation to the DNS total pressure.

3.4.3. *Relation between forces and far-field quantities*

Curle (1955) predicted that the sound generated by the fluctuating forces at the solid boundary will have the same frequency as the fluctuating velocity field. In order to see the relation among the forces, the frequencies of the sound pressure waves and the velocity fluctuations in the far field, plotted in figure 19 are time-histories of the total pressure Δp and the streamwise velocity component u, both taken at the outer boundary of the sound region, $r = 100$. The solid line denotes the data at $\theta = 0°$ and the dashed line denotes the data at $\theta = 90°$. The Mach number is $M = 0.2$. In figure 19(b), the velocity component u is normalized by U_∞. Because the pressure waves propagate at $c_\theta(\theta)$ which is equal to $c_\infty(1 - M\cos\theta)$, the fluctuations plotted in figure 19 may be considered to be generated near the cylinder surface during the time period $t = 1900$–2000 for $\theta = 90°$ and $t = 1875$–1975 for $\theta = 0°$; the corresponding C_L and C_D are shown in figure 4. Figure 19 shows that frequencies of both Δp and u measured at $\theta = 0°$ are the same as the frequency of C_D and those measured at $\theta = 90°$ are the same as that of C_L, in agreement with Curle's prediction.

Figure 19(b) also shows that the mean velocity u, measured on the outer boundary of the sound region, is smaller than unity, at $\theta = 0°$ and larger than unity at $\theta = 90°$; the difference from unity is approximately 0.1% at $r = 100$, $\theta = 0°$. This result demonstrates that the effect of the cylinder reaches far upstream. Therefore, we should be careful if we prescribe $u = 1$ for an upstream boundary condition of the velocity component, though this condition has been widely used.

https://doi.org/10.1017/S0022112002002124 Published online by Cambridge University Press

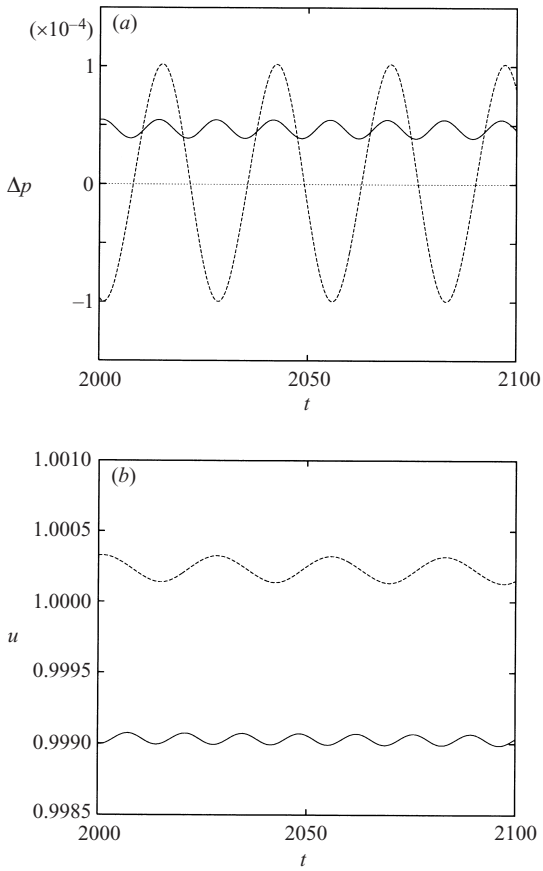


FIGURE 19. Pressure and velocity fluctuations measured in the far field. $r = 100$. $M = 0.2$, $Re = 150$. (a) Total pressure Δp, (b) streamwise velocity component u. ——, $\theta = 0°$; – – – –, $\theta = 90°$.

3.4.4. *Variation with M*

The essential features of the results shown in figures 15 to 19 for $M = 0.2$ and the related discussion are not affected by the Mach number for the Mach number range treated in this paper. For example, the variation of the pressure fields with M is presented in figure 20 for $M = 0.1$ and 0.3. In the figure, the left-hand column shows the results for $M = 0.1$ and the right-hand column for $M = 0.3$. Figure 20(a) shows Curle's solution, $\Delta\tilde{p}_{curle}$, figure 20(b) shows Curle's modified solution, $\Delta\tilde{p}^{D}_{curle}$, and figure 20($c$) shows the DNS fluctuation pressure, $\Delta\tilde{p}$. By comparing figure 20 with figure 15, we can readily see that the characteristic features are not affected by M. Figure 20(b) shows that the propagation angle θ_p of the pulses is well-approximated by the relation $\theta_p = \cos^{-1} M$ in (3.22): $\theta_p = \pm 84.3°$ for $M = 0.1$ and $\pm 72.5°$ for $M = 0.3$.

4. Summary and concluding remarks

The sound generated by a circular cylinder in a flow of $Re = 150$ has been investigated by direct solution of the two-dimensional unsteady compressible Navier–Stokes equations, and the generation and propagation mechanisms of the sound have

https://doi.org/10.1017/S0022112002002124 Published online by Cambridge University Press

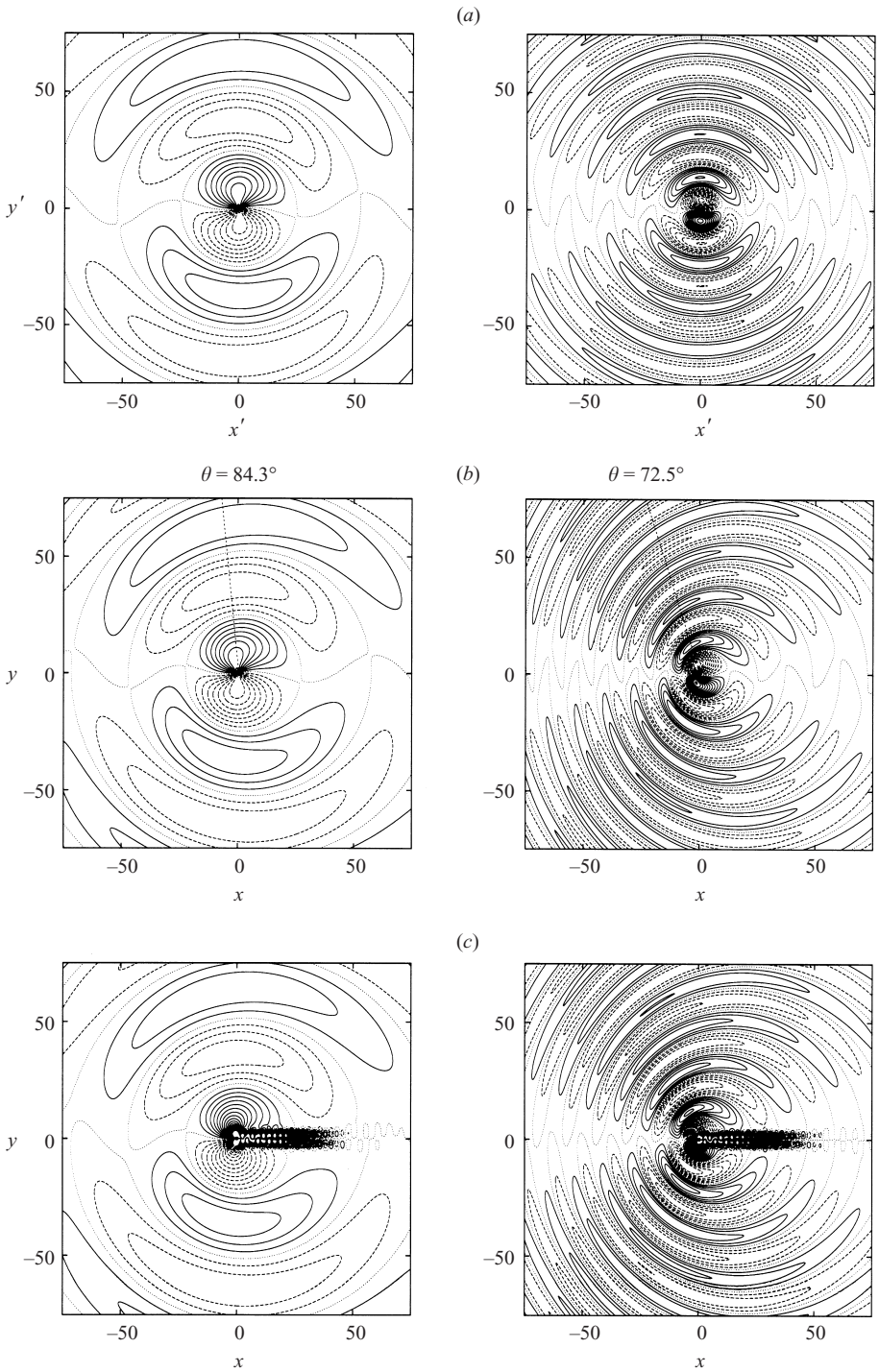


FIGURE 20. Effect of the Mach number on pressure fields. $Re = 150$, $t = 2000$. Left column is for $M = 0.1$, and right column is for $M = 0.3$. (*a*) Curle's solution, $\Delta\tilde{p}_{curle}$, (*b*) Curle's modified solution, $\Delta\tilde{p}^{D}_{curle}$, (*c*) DNS result, $\Delta\tilde{p}$. The contour levels are the same as in figure 15. In figure 20(*b*), the dotted line denotes the propagation angle $\theta_p (= \cos^{-1} M)$.

https://doi.org/10.1017/S0022112002002124 Published online by Cambridge University Press

been clarified in some detail. The results have shown that sound pressure waves are generated primarily by vortex shedding from the cylinder surface into its wake. When a vortex is shed from one side of the cylinder, a negative pressure pulse is generated on that side whereas a positive pressure pulse is generated on the other side; alternate vortex shedding from the upper and lower sides of the cylinder produces negative and positive pulses alternately and thus produces sound pressure waves on both sides. The generated sound has a dipolar nature: the lift dipole dominates the sound field. The Doppler effect has been shown to affect the propagation process. It has been found that the propagation angle of the pressure waves is well-approximated by $\theta_p = \cos^{-1} M$. The DNS results have also confirmed the validity of the scaling law at low Mach numbers, $\Delta\tilde{p} \propto M^{2.5}/r^{0.5}$, which is obtained by an estimation based on Curle's acoustic analogy.

The direct solutions were also compared with the solutions based on Curle's acoustic analogy. The results have shown that Curle's solution well-describes both the generation and propagation mechanisms of the sound and gives a good approximation to the DNS result if the Doppler effect is taken into account. Inclusion of the Doppler effect in Curle's solution is straightforward; we can simply apply the transformation $r' = r/(1 - M\cos\theta)$ or equivalently $c_\theta(\theta) = c_\infty(1 - M\cos\theta)$. It should be also mentioned that Curle's solution does not contain the mean pressure and thus should be interpreted as giving the fluctuation pressure.

The effect of the Reynolds number on the sound generation is left for future study, especially in the case when it is high enough that three-dimensionality should be taken into account.

The authors wish to thank Professor Katsuya Ishii, Nagoya University, for helpful discussions. Thanks are also due to Dr Yuji Hattori, Kyushu Institute of Technology, and Sakari Onuma and Hiroyuki Hosoya, the Institute of Fluid Science, Tohoku University, for useful discussions and technical assistance. The first author expresses his sincere appreciation to Asako Inoue for her continuous encouragement. Computations were performed on the NEC SX-5 at the Institute of Fluid Science, Tohoku University.

Appendix A. Multipole expansions for a uniformly moving source in two dimensions

The wave equation in a uniform medium at the sound speed c_∞ is given by

$$\left(\frac{1}{c_\infty^2}\frac{\partial^2}{\partial t^2} - \nabla^2\right) p(\boldsymbol{x}, t) = \mathscr{F}(\boldsymbol{x}, t). \tag{A 1}$$

Here $\mathscr{F}(\boldsymbol{x}, t)$ is a pressure source and assumed to be acoustically compact around $\boldsymbol{x} = 0$. Then the far-field solution is identified as that generated by the superposition of point multipoles (Howe 1998, § 1.8.3). Both in two and three dimensions, the distributed source $\mathscr{F}(\boldsymbol{x}, t)$ may be replaced with the multipole expansion

$$\sum_{n=0}^{\infty} S^n_{ijk\cdots}(t)\frac{\partial^n \delta(\boldsymbol{x})}{\partial x_i \partial x_j \partial x_k \cdots}, \tag{A 2}$$

where

$$S^n_{ijk\cdots}(t) = \frac{(-1)^n}{n!}\int y_i y_j y_k \cdots \mathscr{F}(\boldsymbol{y}, t)\,\mathrm{d}\boldsymbol{y}.$$

https://doi.org/10.1017/S0022112002002124 Published online by Cambridge University Press

The integral formula (A 1) can be also expanded as

$$p(\boldsymbol{x},t)=\iint_{-\infty}^{\infty}\mathscr{F}(\boldsymbol{y},t')G(\boldsymbol{x}-\boldsymbol{y},t-t')\,\mathrm{d}\boldsymbol{y}\,\mathrm{d}t'\approx\sum_{n=0}^{\infty}p_n(\boldsymbol{x},t), \tag{A 3}$$

where

$$p_n(\boldsymbol{x},t)=\frac{\partial^n}{\partial x_i\partial x_j\partial x_k\cdots}\int_{-\infty}^{\infty}S^n_{ijk\cdots}(t')G(\boldsymbol{x},t-t')\,\mathrm{d}t' \tag{A 4}$$

and G denotes Green's function; p_n is called a multipole of order 2^n (in three dimensions). In two dimensions, the solution (A 4) is given by the two-dimensional Green's function

$$G(\boldsymbol{x}-\boldsymbol{y},t-t')=\frac{H(t-t'-|\boldsymbol{x}-\boldsymbol{y}|/c_\infty)}{2\pi\sqrt{(t-t')^2-|\boldsymbol{x}-\boldsymbol{y}|^2/c_\infty^2}}, \tag{A 5}$$

where H is the Heaviside step function.

If the source is moving at a constant velocity $\boldsymbol{U}$, $\delta(\boldsymbol{x})$ in (A 2) is consistently replaced with $\delta(\boldsymbol{x}-\boldsymbol{U}t)$ by choosing the coordinates $(\boldsymbol{x},t)$ as the source is located at the origin $\boldsymbol{x}=0$ at $t=0$. Let the source-fixed coordinates be defined by $\boldsymbol{r}=\boldsymbol{x}-\boldsymbol{U}t$ and the corresponding multipole by $p_n^D(\boldsymbol{r},t)$. Transforming from the emission time t' to τ' by $t-t'-R/c_\infty=-\tau'$ where $\boldsymbol{R}=\boldsymbol{x}-\boldsymbol{U}t'$ is the emission time coordinate and $R=|\boldsymbol{R}|$, the multipole (A 4) is rewritten

$$p_n^D(\boldsymbol{r},t)=\frac{\partial^n}{\partial x_i\partial x_j\partial x_k\cdots}\int_{-\infty}^{0}\frac{S^n_{ijk\cdots}(t-R/c_\infty+\tau')}{2\pi\sqrt{\tau'^2-2(R/c_\infty)\tau'}}\,\mathrm{d}\tau'. \tag{A 6}$$

Because the integrand is dominated by the neighbourhood of $\tau'=0$, τ'^2 in the square root can be neglected, and R may be replaced with $r'=|\boldsymbol{r}'|$ where $\boldsymbol{r}'=\boldsymbol{x}-\boldsymbol{U}\tau=\boldsymbol{r}+\boldsymbol{U}(t-\tau)$ is the coordinate at time $\tau=t-r'/c_\infty$. The differentiation of $\tau=t-r'(\boldsymbol{x},\tau)/c_\infty$ gives

$$\frac{\partial\tau}{\partial x_i}=-\frac{r'_i}{c_\infty r'(1-M\cos\theta')},$$

where $\boldsymbol{M}=\boldsymbol{U}/c_\infty$, $M=|\boldsymbol{M}|$, and θ' is the angle between $\boldsymbol{U}$ and $\boldsymbol{r}'$. Hence, at $r=|\boldsymbol{r}|\to\infty$, the multipole (A 6) is approximated by

$$p_n^D(\boldsymbol{r},t)\approx\frac{c_\infty^{1/2}}{2^{3/2}\pi r'^{1/2}}\frac{(-1)^n r'_i r'_j r'_k\cdots}{c_\infty^n r'^n(1-M\cos\theta)^n}\int_{-\infty}^{0}\frac{\partial^n S^n_{ijk\cdots}(\tau+\tau')}{\partial\tau^n}\frac{\mathrm{d}\tau'}{\sqrt{-\tau'}} \tag{A 7}$$

in which the Doppler factor is described in terms of the angle θ between $\boldsymbol{U}$ and $\boldsymbol{r}$ by using the relation $1-M\cos\theta'=\sqrt{1-M^2\sin^2\theta}(\sqrt{1-M^2\sin^2\theta}-M\cos\theta)\approx 1-M\cos\theta$. Now the solution p_n for the source at rest is obtained by substituting $M=0$ in (A 7). Thus the relation between p_n^D and p_n in two dimensions is expressed as

$$p_n^D(\boldsymbol{r},t)=\frac{p_n(\boldsymbol{r}',t)}{(1-M\cos\theta)^n}, \tag{A 8}$$

where

$$r'=\frac{r}{\sqrt{1-M^2\sin^2\theta}-M\cos\theta}\approx\frac{r}{1-M\cos\theta}. \tag{A 9}$$

Note that (A 8) gives the expansion relation (3.4) in § 3.2.3, because $p_n(\boldsymbol{r}',t)$ corresponds to $\Delta\tilde{p}_n^M(r',\theta,t)$.

https://doi.org/10.1017/S0022112002002124 Published online by Cambridge University Press

Howe (1998) gives the Doppler effect on multipole of order 2^n in three dimensions as the prefactor $1/(1-M\cos\theta)^{n+1}$, rather than $1/(1-M\cos\theta)^n$ in two dimensions. This difference is because the delta function, contained in the three-dimensional Green's function of (A 1), is the first derivative of the Heaviside function: $\delta(t) = \mathrm{d}H(t)/\mathrm{d}t$. In fact, by using the three-dimensional Green's function $G(\boldsymbol{x}-\boldsymbol{y}, t-t') = \delta(t-t'-|\boldsymbol{x}-\boldsymbol{y}|/c_\infty)/(4\pi|\boldsymbol{x}-\boldsymbol{y}|)$, the three-dimensional multipole is obtained from (A 4) as

$$p_n^D(\boldsymbol{r}, t) \approx \frac{1}{4\pi r'} \frac{(-1)^n r'_i r'_j r'_k \cdots}{c_\infty^n r'^n (1-M\cos\theta)^{n+1}} \frac{\partial^n S^n_{ijk\ldots}(\tau)}{\partial \tau^n}, \tag{A 10}$$

where τ is the solution of $|\boldsymbol{r}+\boldsymbol{U}(t-\tau)| = c_\infty(t-\tau)$, and $\boldsymbol{r}' = \boldsymbol{r}+\boldsymbol{U}(t-\tau)$ and $r' = |\boldsymbol{r}'|$.

Appendix B. Curle's solution in two dimensions

The Lighthill equation (Lighthill 1952) is an exact reformulation of the compressible Navier–Stokes equation:

$$\left(\frac{1}{c_\infty^2}\frac{\partial^2}{\partial t^2} - \nabla^2\right)[c_\infty^2(\rho-\rho_\infty)] = \frac{\partial^2 T_{ij}}{\partial x_i \partial x_j}, \tag{B 1}$$

where

$$T_{ij} = \rho u_i u_j + p'_{ij} - c_\infty^2(\rho-\rho_\infty)\delta_{ij} \tag{B 2}$$

is Lighthill's stress tensor, $p'_{ij} = (p-p_\infty)\delta_{ij} - e_{ij}$ and e_{ij} denotes the viscous stress tensor. Now we assume that a fluid fills a region V except for stationary and rigid enclosed boundaries $S = \partial V$, and that the fluid is at rest at infinity and at S. Then the solution becomes (Goldstein 1976, § 3.2)

$$\begin{aligned} c_\infty^2[\rho(\boldsymbol{x},t)-\rho_\infty] = {} & \frac{\partial^2}{\partial x_i \partial x_j}\int_V \mathrm{d}\boldsymbol{y}\int_{-\infty}^{\infty} T_{ij}(\boldsymbol{y},t')G(\boldsymbol{x},\boldsymbol{y},t-t')\,\mathrm{d}t' \\ & + \frac{\partial}{\partial x_i}\int_S \mathrm{d}S_j(\boldsymbol{y})\int_{-\infty}^{\infty} p'_{ij}(\boldsymbol{y},t')G(\boldsymbol{x},\boldsymbol{y},t-t')\,\mathrm{d}t', \end{aligned} \tag{B 3}$$

where G is Green's function of the Lighthill equation (B 1) and $\mathrm{d}\boldsymbol{S}$ denotes the surface element directed normally from the fluid region V into the region enclosed by the boundary S.

By substituting into (B 3) the two-dimensional Green's function of the Lighthill equation (B 1),

$$G(\boldsymbol{x},\boldsymbol{y},t-t') = \frac{H(t-t'-|\boldsymbol{x}-\boldsymbol{y}|/c_\infty)}{2\pi\sqrt{(t-t')^2-|\boldsymbol{x}-\boldsymbol{y}|^2/c_\infty^2}}, \tag{B 4}$$

where H is the Heaviside step function, we obtain the two-dimensional form of Curle's exact solution as follows:

$$\begin{aligned} c_\infty^2[\rho(\boldsymbol{x},t)-\rho_\infty] = {} & \frac{\partial^2}{\partial x_i \partial x_j}\int_V \mathrm{d}\boldsymbol{y}\int_{-\infty}^{t-|\boldsymbol{x}-\boldsymbol{y}|/c_\infty} \frac{T_{ij}(\boldsymbol{y},t')\,\mathrm{d}t'}{2\pi\sqrt{(t-t')^2-|\boldsymbol{x}-\boldsymbol{y}|^2/c_\infty^2}} \\ & - \frac{\partial}{\partial x_i}\oint_S \mathrm{d}\ell(\boldsymbol{y})\int_{-\infty}^{t-|\boldsymbol{x}-\boldsymbol{y}|/c_\infty} \frac{f_i(\boldsymbol{y},t')\,\mathrm{d}t'}{2\pi\sqrt{(t-t')^2-|\boldsymbol{x}-\boldsymbol{y}|^2/c_\infty^2}}, \end{aligned} \tag{B 5}$$

where $f_i\,\mathrm{d}\ell(\boldsymbol{y}) = -p'_{ij}\,\mathrm{d}S_j(\boldsymbol{y})$ is the force on the fluid in the i-direction exerted by the segment $\mathrm{d}\ell$ at $\boldsymbol{y}$ on the boundary S. If we assume that the source region is compact,

https://doi.org/10.1017/S0022112002002124 Published online by Cambridge University Press

then $|\boldsymbol{x}-\boldsymbol{y}|$ in the integrals can be replaced by $|\boldsymbol{x}|$. By defining the retarded time to be $\tau = t - |\boldsymbol{x}|/c_\infty$ and transforming the time-integral variable to $t' = \tau' + \tau$, the spatial derivatives may be replaced with the time derivatives as $\partial/\partial x_i = -c_\infty^{-1}(x_i/|\boldsymbol{x}|)\partial/\partial\tau$. Then, under the assumption of isentropic flow, $p - p_\infty = c_\infty^2(\rho - \rho_\infty)$, (B 5) is reduced to

$$p(\boldsymbol{x},t) - p_\infty = \frac{x_i x_j}{2^{3/2}\pi c_\infty^{3/2}|\boldsymbol{x}|^{5/2}} \int_{-\infty}^{0} \left[\frac{\partial^2}{\partial\tau^2}\int_V T_{ij}(\boldsymbol{y},\tau+\tau')\,\mathrm{d}\boldsymbol{y}\right]\frac{\mathrm{d}\tau'}{\sqrt{-\tau'}}$$
$$+ \frac{x_i}{2^{3/2}\pi c_\infty^{1/2}|\boldsymbol{x}|^{3/2}} \int_{-\infty}^{0} \left[\frac{\partial}{\partial\tau}\oint_S f_i(\boldsymbol{y},\tau+\tau')\,\mathrm{d}\ell(\boldsymbol{y})\right]\frac{\mathrm{d}\tau'}{\sqrt{-\tau'}}, \qquad \text{(B 6)}$$

where the τ'^2 terms in the integrands are neglected because the integrals with respect to τ' are mainly contributed in the neighbourhood of $\tau' = 0$. Finally, by replacing $\partial/\partial\tau$ with $\partial/\partial\tau'$ in the square brackets and by using the retransformation $\tau' = t' - \tau$, we obtain an expression which is identical to (3.13).

REFERENCES

Cimbala, J. M., Nagib, H. M. & Roshko, A. 1988 Large structure in the far wakes of two-dimensional bluff bodies. *J. Fluid Mech.* **190**, 265–298.

Colonius, T., Lele, S. K. & Moin, P. 1994 The scattering of sound waves by a vortex: numerical simulation and analytical solutions. *J. Fluid Mech.* **260**, 271–298.

Colonius, T., Lele, S. K. & Moin, P. 1997 Sound generation in a mixing layer. *J. Fluid Mech.* **330**, 375–409.

Cox, J. S., Brentner, K. S. & Rumsey, C. L. 1998 Computation of vortex shedding and radiated sound for a circular cylinder: subcritical to transonic Reynolds numbers. *Theoret. Comput. Fluid Dyn.* **12**, 233–253.

Curle, N. 1955 The influence of solid boundaries upon aerodynamic sound. *Proc. R. Soc. Lond.* A **231**, 505–514.

Etkin, B., Korbacher, G. K. & Keefe, R. T. 1957 Acoustic radiation from a stationary cylinder in a finite stream (aeolian tones). *J. Acoust. Soc. Am.* **29**, 30–36.

Fey, U., König, M. & Eckelmann, H. 1998 A new Strouhal–Reynolds-number relationship for the circular cylinder in the range $47 < Re < 10^5$. *Phys. Fluids* **10**, 1547–1549.

Ffowcs Williams, J. E. 1969 Hydrodynamic noise. *Annu. Rev. Fluid Mech.* **1**, 197–222.

Ffowcs Williams, J. E. 1977 Aeroacoustics. *Annu. Rev. Fluid Mech.* **9**, 447–468.

Ffowcs Williams, J. E. 1996 Aeroacoustics. *J. Sound Vib.* **190**, 387–398.

Gerrard, J. H. 1955 Measurements of the sound from circular cylinders in an air stream. *Proc. Phys. Soc. Lond.* B **68**, 453–461.

Goldstein, M. E. 1976 *Aeroacoustics.* McGraw-Hill.

Hansen, R. P., Long, L. N. & Morris, P. J. 2000 Unsteady, laminar flow simulations using the nonlinear disturbance equations. *AIAA Paper* 2000-1981.

Hardin, J. C. & Lamkin, S. L. 1984 Aeroacoustic computation of cylinder wake flow. *AIAA J.* **22**, 51–57.

Hardin, J. C. & Pope, D. S. 1994 An acoustic/viscous splitting technique for computational aeroacoustics. *Theor. Comp. Fluid Dyna.* **6**, 323–340.

Howe, H. S. 1998 *Acoustics of Fluid-Structure Interactions.* Cambridge University Press.

Inoue, O. 2000 Propagation of sound generated by weak shock–vortex interaction. *Phys. Fluids* **12**, 1258–1261.

Inoue, O. & Hattori, Y. 1999 Sound generation by shock-vortex interactions. *J. Fluid Mech.* **380**, 81–116.

Inoue, O., Hattori, Y. & Sasaki, T. 2000 Sound generation by coaxial collision of two vortex rings. *J. Fluid Mech.* **424**, 327–365.

Inoue, O. & Takahashi, Y. 2000 Successive generation of sounds by shock–strong vortex interaction. *Phys. Fluids* **12**, 3229–3234.

https://doi.org/10.1017/S0022112002002124 Published online by Cambridge University Press

Inoue, O. & Yamazaki, T. 1999 Secondary vortex streets in two-dimensional cylinder wakes. *Fluid Dyn. Res.* **25**, 1–18.

Kambe, T. & Minota, T. 1983 Acoustic wave radiated by head-on collision of two vortex rings. *Proc. R. Soc. Lond.* A **386**, 277–308.

Kwon, K. & Choi, H. 1996 Control of laminar vortex shedding behind a circular cylinder using splitter plates. *Phys. Fluids* **8**, 479–486.

Landau, L. D. & Lifshitz, E. M. 1987 *Fluid Mechanics*, 2nd edn. Course of Theoretical Physics, vol. 6. Pergamon.

Lele, S. K. 1992 Compact finite difference schemes with spectral-like resolution. *J. Comput. Phys.* **103**, 16–42.

Lele, S. K. 1997 Computational aeroacoustics: a review. *AIAA Paper* 97-0018.

Lighthill, M. J. 1952 On sound generated aerodynamically: I. General theory. *Proc. R. Soc. Lond.* A **221**, 564–587.

Mankbadi, R. R., Hayder, M. H. & Povinelli, L. A. 1994 Structure of supersonic jet flow and its radiated sound. *AIAA J.* **32**, 897–906.

Manoha, E., Troff, B. & Sagaut, P. 2000 Trailing-edge noise prediction using large-eddy simulation and acoustic analogy. *AIAA J.* **38**, 575–583.

Minota, T. & Kambe, T. 1986 Observation of acoustic emission from head-on collision of two vortex rings. *J. Sound Vib.* **111**, 51–59.

Mitchell, B. E., Lele, S. K. & Moin, P. 1995 Direct computation of the sound from a compressible co-rotating vortex pair. *J. Fluid Mech.* **285**, 181–202.

Mitchell, B. E., Lele, S. K. & Moin, P. 1999 Direct computation of the sound generated by vortex pairing in an axisymmetric jet. *J. Fluid Mech.* **383**, 113–142.

Moin, P. & Mahesh, K. 1998 Direct numerical simulation: a tool in turbulence research. *Annu. Rev. Fluid Mech.* **30**, 539–578.

Oertel, Jr, H. 1990 Wakes behind blunt bodies. *Annu. Rev. Fluid Mech.* **22**, 539–564.

Park, J., Kwon, K. & Choi, H. 1998 Numerical solutions of flow past a circular cylinder at Reynolds numbers up to 160. *KSME Intl J.* **12**, 1200–1205.

Phillips, O. M. 1956 The intensity of aeolian tones. *J. Fluid Mech.* **1**, 607–624.

Pointsot, T. & Lele, S. K. 1992 Boundary conditions for direct simulation of compressible viscous flows. *J. Comput. Phys.* **101**, 104–129.

Pope, D. S. 1997 A viscous/acoustic splitting technique for aeolian tone prediction. *Proc. Second Computational Aeroacoustics* (*CAA*) *Workshop on Benchmark Problems* (ed. C. K. W. Tam & J. C. Hardin). NASA CP-3352, pp. 305–318.

Rayleigh, Lord 1896 *The Theory of Sound*, Vols. I & II. Macmillan.

Shen, W. Z. & Sørensen, J. N. 1999 Comment on the aeroacoustic formulation of Hardin and Pope. *AIAA J.* **37**, 141–143.

Slimon, S. A., Soteriou, M. C. & Davis, D. W. 1999 Computational aeroacoustics simulations using the expansion about incompressible flow approach. *AIAA J.* **37**, 409–416.

Strouhal, V. 1878 Ueber eine besondere art der tonerregung. *Annu. Phys. Chem.* (*Wied. Annu. Phys.*) **5**, 216–251.

Tam, C. K. W. 1995 Computational aeroacoustics: issues and methods. *AIAA J.* **33**, 1788–1796.

Tam, C. K. W. & Hardin, J. C. (Eds.) 1997 *Proc. Second Computational Aeroacoustics* (*CAA*) *Workshop on Benchmark Problems*. NASA CP-3352.

Wang, M., Lele, S. K. & Moin, P. 1996*a* Computation of quadrupole noise using acoustic analogy. *AIAA J.* **34**, 2247–2254.

Wang, M., Lele, S. K. & Moin, P. 1996*b* Sound radiation during local laminar breakdown in a low Mach number boundary layer. *J. Fluid Mech.* **319**, 197–218.

Williamson, C. H. K. 1989 Oblique and parallel modes of vortex shedding in the wake of a circular cylinder at low Reynolds numbers. *J. Fluid Mech.* **206**, 579–627.

Williamson, C. H. K. 1996 Vortex dynamics in the cylinder wake. *Annu. Rev. Fluid Mech.* **28**, 477–539.

Williamson, C. H. K. & Prasad, A. 1993 A new mechanism for oblique wave resonance in the 'natural' far wake. *J. Fluid Mech.* **256**, 269–313.

You, D., Choi, H., Choi, M.-R. & Kang, S.-H. 1998 Control of flow-induced noise behind a circular cylinder using splitter plates. *AIAA J.* **36**, 1961–1967.

https://doi.org/10.1017/S0022112002002124 Published online by Cambridge University Press